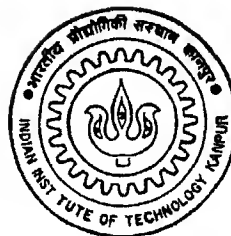


IMAGE RECONSTRUCTION USING HAAR FILTER & WAVELET PRE-PROCESSING

by

Sanjay G Joshi



DEPARTMENT OF ELECTRICAL ENGINEERING

INDIAN INSTITUTE OF TECHNOLOGY KANPUR

January, 1996

EE
1996
M
JOS
IME

IMAGE RECONSTRUCTION USING HAAR FILTER & WAVELET PRE-PROCESSING

A Thesis Submitted
in Partial Fulfillment of the Requirements
for the Degree of
Master of Technology

by
Sanjay G. Joshi

to the
DEPARTMENT OF ELECTRICAL ENGINEERING
INDIAN INSTITUTE OF TECHNOLOGY, KANPUR

January 1996

21 MAR 1996
CENTRAL LIBRARY
IIT KANPUR
444 No. A 121212

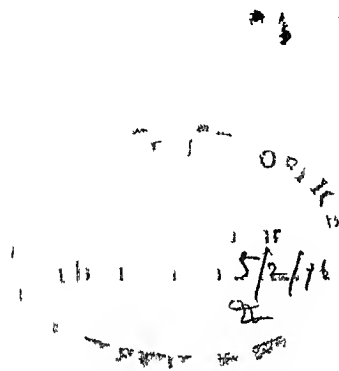
EE-1996-M-305-IMA



A121212

CERTIFICATE

This is to certify that Mr Sunjay C Joshi Roll No 9110415 has carried out the thesis work titled "IMAGE RECONSTRUCTION USING HARRIS CORNER & WAVELET TRANSFORM PROCESSING" under my supervision and the same is not submitted elsewhere for a degree



Ray
5 2 96

Dr C C Ray

Prof Dept of EE

(Thesis Supervisor)

ACKNOWLEDGEMENT

I take this opportunity to express my sincere gratitude towards my thesis supervisor Dr. C. C. Ray. He allowed me to work in the area of my interest, was always available whenever I needed him, patiently listened to my doubts, and always encouraged me to carry out different experiments.

I also wish to thank all my friends from IIT Department and from Hall 3 & Hall 1. Special thanks goes to Comathishan, a, Devendra, Abhinav, Basha, Prashant, Reddy, Hemant and Mukul who made my 18 months stay very much enjoyable.

Sanjay C. Joshi

Dedicated to

AIE

and

BABA

ABSTRACT

Among all the tomographic reconstruction techniques, convolution backprojection is the most widely used technique. The low pass window function used in this method plays an important role in the overall quality of the reconstructed image as the noise suppression and spatial resolution are determined by the window function. The Ham filter is a recent development in the filters used for image reconstruction. In this work we have used the Ham filter in combination with wavelet transform based space variant noise suppression technique. Computer simulation results show that the Ham filter gives better results as compared to conventional filters like Ram Lak, Shepp Logan, Generalized Hamming, etc.

Contents

1	Introduction	5
1.1	Review	5
1.2	Organization of Thesis	6
2	Basic concepts	8
2.1	Introduction	8
2.2	Discretization of the reconstruction problem	9
2.3	Algebraic techniques	10
2.4	Transform domain methods	11
2.5	Discrete Implementation of Inverse Radon Transform	14
2.5.1	Fourier Domain Reconstruction Methods	15
2.6	Fan Beam Reconstruction	16
3	Haar Filter	18
3.1	Introduction to Haar filter	18
3.2	Discrete Haar filter	22
4	Wavelet Transform	29
4.1	Introduction	29
4.2	Discrete Parameter Wavelet Transform	30
4.3	Wavelets and Multiresolution Analysis	31
4.4	Fast Wavelet Transform	34
4.5	Compactly supported orthonormal basis	34
5	Wavelets in Tomography	37
5.1	Review	37
5.2	Space varying filtering	37

5.3	Selecting the threshold	38
6	Simulation results	41
6.1	Standard Reconstruction	44
6.2	Reconstruction from Noisy projections	50
6.3	Conclusion	55
A		56

List of Figures

2.1	Radon transform as a line integral	9
2.2	Frequency response of different convolvers	14
2.3	Grid Structures	15
2.4	Parallel beam and fan beam geometry	16
2.5	Parallel beam projections	16
3.1	2D Hough function and it's projection	19
3.2	Plot of $W_{0\Delta}(\xi, \theta)$	22
3.3	$k_d(n, 0) \rho = 2$	24
3.4	$k_d(n, \pi/12) \rho = 2$	25
3.5	$k_d(n, \pi/6) \rho = 2$	25
3.6	$k_d(n, \pi/4) \rho = 2$	26
3.7	$k_d(n, 0) \rho = 4$	26
3.8	$k_d(n, \pi/12) \rho = 4$	27
3.9	$k_d(n, \pi/6) \rho = 4$	27
3.10	$k_d(n, \pi/4) \rho = 4$	28
4.1	Dyadic grid for discretization of (a, τ)	31
4.2	2 channel perfect reconstruction quadrature mirror filter bank	33
4.3	Pyramidal algorithm Analysis section	34
4.4	Pyramidal algorithm Synthesis section	34
4.5	Scaling function for Daub 4 filter	35
4.6	Wavelet for Daub 4 filter	35
4.7	Scaling function for Daub 8 filter	36
4.8	Wavelet for Daub 8 filter	36
6.1	MSL Vs M with constant N	42

6.2	Cross sectional view along edge	11
6.3	Square reconstruction using Ram Lak filter $\rho = 2$	15
6.4	Square reconstruction using Shepp Logan filter $\rho = 2$	15
6.5	Square reconstruction using Generalized Hamming filter $\rho = 2$	46
6.6	Square reconstruction using Ham filter $\rho = 2$	16
6.7	Square reconstruction using Ram Lak filter $\rho = 4$	17
6.8	Square reconstruction using Shepp Logan filter $\rho = 4$	17
6.9	Square reconstruction using Generalized Hamming filter $\rho = 4$	18
6.10	Square reconstruction using Ham filter $\rho = 4$	18
6.11	Phantom reconstruction using Generalized Hamming filter $\rho = 1$	19
6.12	Phantom reconstruction using Ham filter $\rho = 1$	19
6.13	Noisy square reconstruction using wavelet pre processing and Ram Lak filter $\rho = 1$	52
6.14	Noisy square reconstruction using wavelet pre processing and Shepp Logan filter $\rho = 1$	52
6.15	Noisy square reconstruction using wavelet pre processing and Generalized Hamming filter $\rho = 1$	53
6.16	Noisy square reconstruction using wavelet pre processing and Ham filter $\rho = 4$	53
6.17	Noisy phantom reconstruction using wavelet pre processing and Generalized Hamming filter $\rho = 4$	54
6.18	Noisy phantom reconstruction using wavelet pre processing and Ham filter $\rho = 4$	54
A.1	Continuity of $w_{0\Delta}(s, \theta)$	56

Chapter 1

Introduction

1.1 Review

The field of transmission and emission tomography has grown extensively in last two decades. Dr Hounsfield developed world's first practical CT scanner in 1970. This brought up a new revolution in the field of medical diagnosis and the techniques like Computerized Tomography (CT), Magnetic Resonance Imaging (MRI), Positron Emission Tomography (PET), Single Photon Emission Tomography (SPECT), etc, are most widely used clinical and experimental tools. The success of these techniques lies in their ability to map some property of internal cross section of the object without macroscopically damaging the object. This obviously leads to many interesting applications in medical diagnosis. There are many other divergent fields such as radio astronomy, electron microscopy [1],[2] etc, which employ essentially the same techniques. A common feature of all these problems is that a set of data is available that is related to the cross sectional properties in a known way, but not related straightforwardly. The objective then is, using this set of collected data, to estimate the mapping of the property along the cross section.

In radio astronomy, the objective is to estimate the electron charge density distribution and magnetic field intensity distribution around the outer structure of the sun [3]. The data collected using the radio telescope array is in the form of strip integrals and the 3D image reconstruction problem is to be solved [3].

The tomographic techniques can broadly be classified in two categories, namely, transmission tomography and emission tomography [1]. In transmission tomography the physi-

cal property evaluated is X ray absorption coefficient while in emission tomography, the physical property evaluated is photon emission intensity, also called as activation function. Although the techniques of data collection used in these two methods are considerably different, the image reconstruction problem fall under the same mathematical formulation.

In CT scanning X rays are passed through the surface under investigation to obtain one dimensional projection at various angles which are then sampled at uniform interval. The data collected is normally contaminated with noise, owing to statistical nature of photon emission [2]. These projections are convolved with a ramp filter and the well known backprojection technique is applied on the filtered projections to reconstruct the cross section. The ramp filter tends to amplify the high frequency components of data as well as noise, but the noise usually dominates at high frequencies. Hence the ramp filter is typically combined with a low pass filter to avoid amplification of the high frequency noise. The low pass filtering is also essential to avoid the aliasing which otherwise results due to the finite value of sampling rate. Too much low pass filtering will result in loss of spatial resolution. The filters like Ram Lak, Shepp Logan, Generalized Hamming etc [4] are the most commonly used filters for these applications.

Recently a new kind of low pass filter based on Haar function was described in [8]. This filter is angle dependent. Another emerging mathematical theory which has found interesting applications in many engineering branches and in physics, is the theory of wavelets. Wavelets have been applied successfully in various signal processing problems such as speech and image data compression, noise removal, edge detection, etc. In tomographic applications wavelets have been used to construct small regions with reduced projection data [5], space variant noise filtering [9-10] etc. The Haar filter, when combined with the wavelet transform based nonlinear space variant noise filtering have shown to yield better quality of the reconstructed image. This claim is verified through computer simulation.

1.2 Organization of Thesis

- Chapter 2 describes the basic principles of transmission tomography. It also describes in brief the two main types of reconstruction techniques, i.e. transform domain and algebraic techniques.

- Chapter 3 describes the theory behind the Ham filter. The relevant equations are also derived in this chapter.
- Chapter 4 gives a brief account of the wavelet transform theory.
- Chapter 5 describes the applications of wavelet transform in tomography. The emphasis will be on spatially varying nonlinear filtering using wavelet transform.
- Chapter 6 presents the results of computer simulation.

Chapter 2

Basic concepts

2.1 Introduction

Consider the space limited function $u(x, y)$ as shown in fig 2.1. We define a new function $g(s, \theta)$ such that

$$g(s, \theta) = \int_{-\infty}^{\infty} \int_{-\infty}^{\infty} u(x, y) \delta(x \cos \theta + y \sin \theta - s) dx dy \quad (2.1)$$

where the delta function $\delta(x)$ has following properties

$$\delta(x) = 0, x \neq 0$$

$$\int_{-\infty}^{\infty} \delta(x) dx = 1 \quad (2.2)$$

$$\int_{-\infty}^{\infty} \delta(\tau - \tau) f(\tau) d\tau = f(\tau)$$

$g(s, \theta)$ is called the Radon transform of $u(x, y)$ and is also referred to as projection of $u(x, y)$ at an angle θ . Thus from eq 2.1 and the properties of $\delta(x)$ we note that only those points (x, y) contribute to the integral which lay on the line P . From fig 2.1, using the rotated co ordinate system we get

$$x = s \cos \theta - y \sin \theta$$

$$y = s \sin \theta + x \cos \theta \quad (2.3)$$

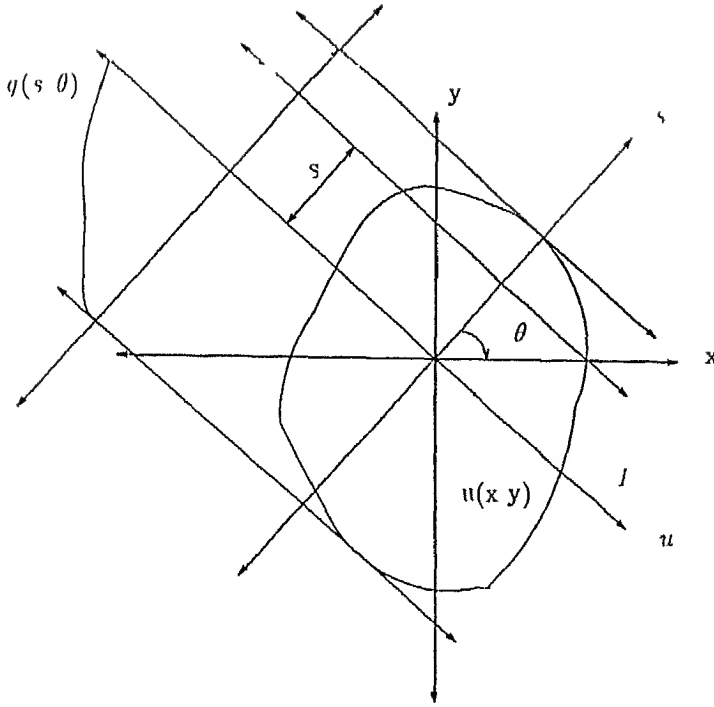


Figure 2.1 Radon transform as a line integral

Using the above equation and the sampling property of the delta function (eq 2.3) we get

$$g(s, \theta) = \int_{-\infty}^{\infty} u(s \cos \theta - u \sin \theta, s \sin \theta + u \cos \theta) du \quad (2.4)$$

In practice these ray integrals are obtained by passing X rays through the object under test and the function $u(x, y)$ represents the distribution of the X ray absorption coefficient. (In case of PET & SPECT, $u(x, y)$ represents the activity distribution [1]). The problem is then that of inversion or finding the function $u(x, y)$ given the projections $g(s, \theta)$ for all values of θ in the range $[0, \pi]$.

2.2 Discretization of the reconstruction problem

In practice the projections are obtained over a discrete set of angles and each projection is sampled at equally spaced points. Let $g_n(m)$ denote the sampled projections. The discrete projections are thus defined as

$$g(n) = g(m + d \frac{n + \pi}{N}) \quad (2.5)$$

$$n \in \{0, 1, 2, \dots, N-1\}$$

$$m \in \{-M, -M+1, \dots, -1, 0, 1, \dots, M\}$$

and $\frac{1}{T}$ is the sampling rate in projection domain and is selected such that

$$d = \frac{D}{M} \quad (2.6)$$

D specifies the boundary of the region within which $g(s, \theta)$ is defined i.e. $g(s, \theta) = 0 \forall \theta$ if $|s| > D$. Also the estimate of the function $u(r, y)$ is evaluated at discrete values of r & y which are spaced at uniform interval. Two methods are used for the computation of $u(x, y)$ algebraic reconstruction techniques and transform domain methods.

2.3 Algebraic techniques

Let us assume that the function $u(r, y)$ can be expressed by a finite series of the form

$$u(r, y) = \sum_{j=0}^{P-1} y_j f_j(x, y) \quad (2.7)$$

where $f_j(r, y)$ are known functions, typically rectangular functions with nonoverlapping region of support as described in [6]. The coefficients $\{y_j\}$ in the series expansion, then characterize the function $u(r, y)$ completely. Let R_j denote the Radon transform operator corresponding to the j^{th} projection sample g_j . Using the linearity property of the Radon transform we get

$$R_j u(r, y) = \sum_{j=0}^{P-1} y_j R_j f_j(x, y) \quad (2.8)$$

or

$$g_j = \sum y a_{j,i} \quad (2.9)$$

where

$$a_{j,i} = R_j f(x_i, y_i) \quad (2.10)$$

Let G denote the column vector of the sampled projections and let Y denote the vector of coefficients in the series expansion. Then the problem can be modeled as that of solving the system of simultaneous equation

$$G = AY \quad (2.11)$$

The matrix A is typically a rectangular matrix with very large size (Of the order of $10^4 \times 10^5$ or more). This makes it virtually impossible to invert the matrix A and hence iterative techniques are used for the solution of the vector Y . The vector Y is given a initial value and at each iteration some correction term is applied to Y so that the vector Y converges to, or is close to the solution of equation discussed in [6]. There are various types of iterative techniques such as additive ART and multiplicative ARI. These methods differ in the manner in which the corrective term is applied to Y [6]. The main drawback of the iterative techniques is that they demand much computational load and the rate of convergence is very slow. Hence the Algebraic reconstruction methods are rarely used although they give better quality of the reconstructed image than the transform domain method when the no. of projection angles are few or when the projections are incomplete [6]. These kind of situations occur, for example, in fast cardiac imaging or in 3D image reconstruction.

2.4 Transform domain methods

All of the Transform Domain methods are based on the inversion formulae developed by John Radon in 1917. The following conventions are used in the discussion to follow and in subsequent chapters.

Small letters (eg g, u etc.) are used to denote the functions (of one variable or two variables) in space domain and capital letters are used to denote the functions in

frequency domain. Thus $G(\xi, \theta)$ denote one dimensional fourier transform of $g(s, \theta)$

$$G(\xi, \theta) = \int_{-\infty}^{\infty} g(s, \theta) e^{-j2\pi \xi s} ds \quad (2.12)$$

The two dimensional fourier transform of $u(x, y)$ is similarly defined as

$$U(\xi_1, \xi_2) = \int_{-\infty}^{\infty} \int_{-\infty}^{\infty} u(x, y) e^{-j2\pi(x\xi_1 + y\xi_2)} dx dy \quad (2.13)$$

and the inverse fourier transforms are given by

$$g(s, \theta) = \int_{-\infty}^{\infty} G(\xi, \theta) e^{j2\pi s\xi} d\xi \quad (2.14)$$

and

$$u(x, y) = \int_{-\infty}^{\infty} \int_{-\infty}^{\infty} U(\xi_1, \xi_2) e^{j2\pi(x\xi_1 + y\xi_2)} d\xi_1 d\xi_2 \quad (2.15)$$

We denote the polar representation of a function of two variables by putting a hat on it. Thus

$$u(r, \psi) = u(r \cos \psi, r \sin \psi) \quad (2.16)$$

$$U(\xi, \phi) = U(\xi \cos \phi, \xi \sin \phi) \quad (2.17)$$

Thus the Fourier transform and the inverse Fourier transforms can also be expressed as

$$U(\xi, \phi) = \int_0^{\infty} \int_0^{2\pi} u(r, \psi) e^{-j2\pi \xi r \cos(\phi - \psi)} r dr d\psi \quad (2.18)$$

$$u(r, \psi) = \int_0^{\infty} \int_0^{2\pi} U(\xi, \phi) e^{j2\pi \xi r \cos(\phi - \psi)} \xi d\xi d\phi \quad (2.19)$$

For the function $U(\xi, \phi)$ we have the symmetry relation

$$U(-\xi, \phi - \pi) = U(\xi, \phi) \quad (2.20)$$

Using this relation it can be shown that

$$u(r, \psi) = \int_{-\infty}^{\infty} \int_0^{\pi} U(\xi, \phi) e^{j2\pi\xi (r\cos\psi - \phi)|\xi|} d\xi d\phi \quad (2.21)$$

According to the central slice theorem [4] we get

$$\begin{aligned} C(\xi, \theta) &= U(\xi, \theta) \\ &= U(\xi \cos \theta, \xi \sin \theta) \end{aligned} \quad (2.22)$$

combining the results we get

$$u(r, \psi) = \int_0^{\pi} \int_{-\infty}^{\infty} C(\xi, \theta) e^{j2\pi(x \cos \theta + y \sin \theta)\xi} |\xi| d\xi d\theta \quad (2.23)$$

In the above equation the innermost integral w.r.t. ξ can be interpreted as filtering the projections with a ramp filter while the outer integral w.r.t. θ is the backprojection operation. Let β denote the backprojection operator. Thus we get

$$\beta g = \int_0^{\pi} g(r \cos \theta + y \sin \theta) d\theta \quad (2.24)$$

The ramp filter tends to amplify high frequency noise and is unstable, hence it is typically combined with a low pass window function $W(\xi)$ and the inverse relation becomes

$$u(x, y) = \int_0^{\pi} \int_{-\infty}^{\infty} G(\xi, \theta) e^{j2\pi(x \cos \theta + y \sin \theta)\xi} W(\xi) |\xi| d\xi d\theta \quad (2.25)$$

$$= \beta P g \quad (2.26)$$

where

$$P g = \int_{-\infty}^{\infty} C(\xi, \theta) e^{j2\pi s \xi} W(\xi) |\xi| d\xi \quad (2.27)$$

$$= g(s, \theta) * w(s)$$

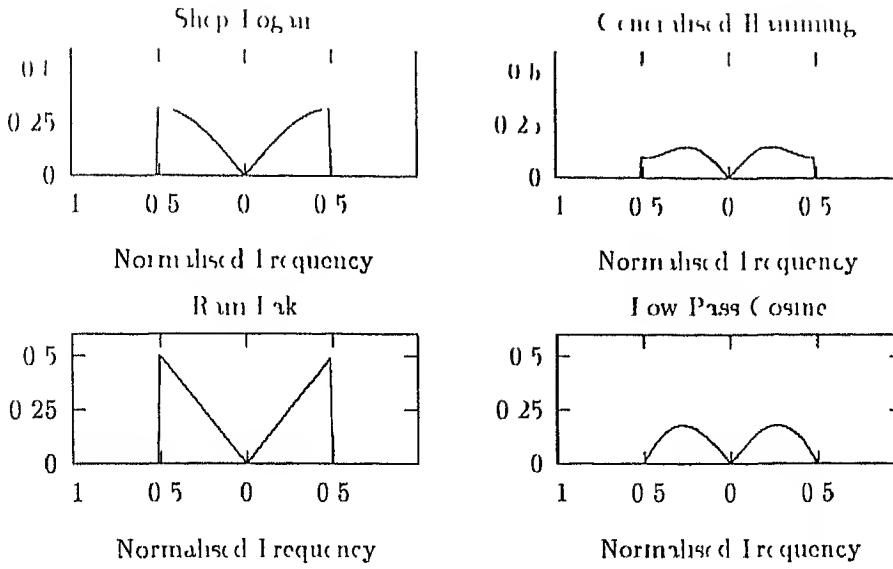


Figure 2.2 Frequency response of different convolvers

$w(s)$ is the one dimensional inverse fourier transform of $W(\xi)|\xi|$

Various windows have been proposed in literature and the most widely used windows are Ram Lak, Shep Logan, Generalized Hamming and Low pass cosine. The plot of $W(\xi)|\xi|$ for all these window functions are shown in fig 2.2

2.5 Discrete Implementation of Inverse Radon Transform

The impulse response of the convolver $w(t)$ is obtained by inverse transforming $W(\xi)$ and the discrete convolver is obtained by sampling the continuous version with proper sampling rate [4]

Let $w(m)$ denote the discrete convolver and let us denote the filtered projections by $\tilde{g}_n(m)$. Then

$$\tilde{g}_n(m) = \sum_{k=-M}^M g_n(m-k)w(k) \quad (2.29)$$

As the function $g_n(m)$ is defined for integer values of m , the value of the projection at other values of m is evaluated by interpolation. Linear interpolation is widely used in practice [4]

Thus let p_i denote the integer part of a real number p and let p_f denote the fractional part of p . Hence $p \in \mathbb{Z}$ and $0 < p_f < 1$. For linear interpolation, the interpolated projection $g_n(p)$ is defined as

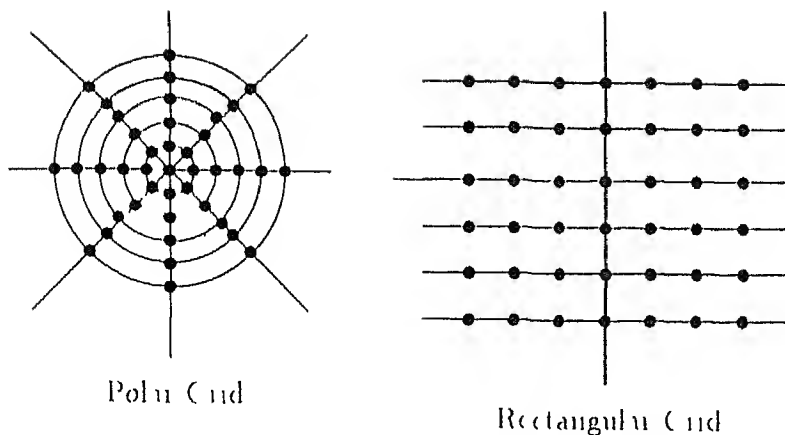


Figure 2.3 Grid Structures

$$q_1(m) = (1 - m_f)q_0(m) + m_f q_0(1 + m) \quad (2.30)$$

The backprojection operator is then discretized and the discretized estimate of the function $u(r, \theta)$ is obtained as

$$u_l(k, l) = \frac{\pi}{N} \sum_{n=0}^{N-1} q_n(p(k \cos(\frac{n\pi}{N}) + l \sin(\frac{n\pi}{N}))) \quad (2.31)$$

where $\frac{1}{N}$ is the sampling rate in spatial domain and $(k, l) \in \mathbb{Z}^2$

The Ram-Lak filter has sharp cut off. This results in high overshoot and ringing in the region of high contrast. The other filters have comparatively smooth roll off.

2.5.1 Fourier Domain Reconstruction Methods

Another transform domain technique not so widely used is the Fourier domain reconstruction method [7]. In this method the projections are Fourier transformed. This gives the 2D Fourier transform of $u(r, \theta)$ sampled on a polar grid as shown in fig 2.3. The polar grid data is converted to rectangular grid data using interpolation and the 2D inverse FFT is taken so as to obtain samples of $u(r, \theta)$ over a rectangular grid. Various interpolation techniques are proposed to convert polar grid data to rectangular grid [7]. The interpolation error is the main source of error. Hence filtered backprojection technique is preferred over Fourier domain reconstruction methods.

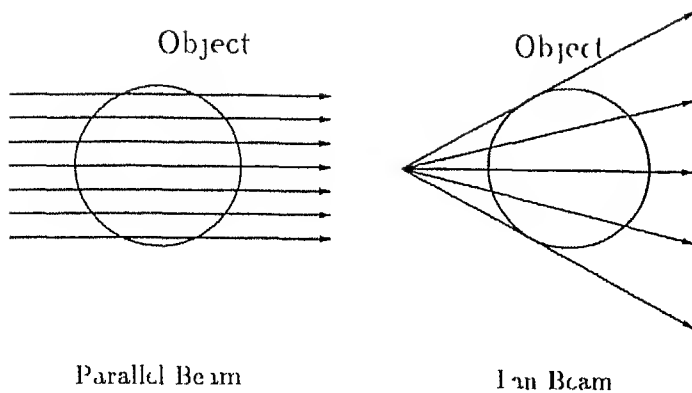


Figure 2.4 Parallel beam and fan beam geometry

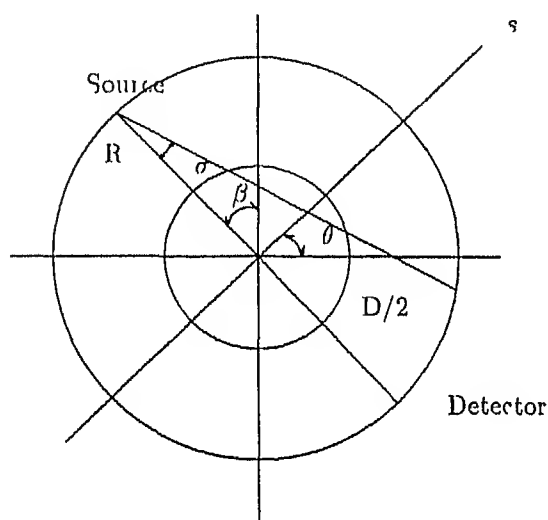


Figure 2.5 Fan beam projections

2.6 Fan Beam Reconstruction

The reconstruction geometry, considered so far, is called parallel beam geometry. Another method widely used in practice due to its simplicity is the fan beam geometry. The details are shown in fig 2.4.

In fan beam geometry, the source moves in a circle of radius R , while the object is in concentric circle of radius $D/2$. The detector is either in the same circle as that of the source or in a circle of different radius, and is diagonally opposite to the source as shown in fig 2.5.

The cone beam projection is denoted by $b(\sigma, \beta)$ where $\sigma \in [-\nu, \nu]$, $0 \leq \beta < 2\pi$ and $\nu = \arcsin(\frac{D}{2R})$.

A fan beam projection data is always some parallel beam data. Thus from fig 2.5 we get

$$b(\sigma, \beta) = g(R \sin \sigma, \sigma + \beta) \quad (2.32)$$

$$g(s, \theta) = b\left(\arcsin \frac{s}{R}, \theta - \arcsin \frac{s}{R}\right) \quad (2.33)$$

Thus the parallel beam reconstruction method can be applied. This is called as method of *rebinning*. Direct reconstruction methods are also possible [3].

A square image and the Shep-Logan Phantom [11] are used in simulation. The results are presented in chap 6.

Chapter 3

Haar Filter

3.1 Introduction to Haar filter

The filters mentioned in chapter 2 are all band limited (in other words they are all having finite region of support in frequency domain) and hence they can not be space limited. The band limited filters allow one to avoid the aliasing when the sampling rate is properly chosen so as to satisfy Shannon's criteria, but in practice the projections are not low pass filtered prior to sampling (although the sensing device provides some sort of low pass filtering, it is not adequate), hence aliasing is always present to some extent in the sampled projections. On the other hand the Haar filter has finite region of support in spatial domain resulting in some aliasing, which can be controlled by oversampling ratio ρ (see next section). The overall effect is a better quality of reconstructed image.

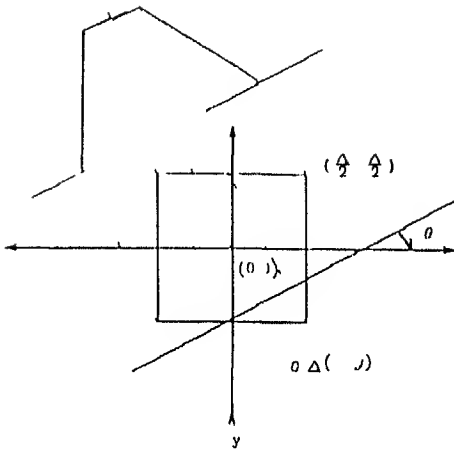


Figure 3.1 2D Haar function and its projection

Consider the 2D Haar function $s_{0\Delta}(x, y)$ as shown in fig 3.1. This function is defined as

$$s_{0\Delta}(x, y) = s_{0\Delta}(x) s_{0\Delta}(y) \quad (3.1)$$

and the function $s_{0\Delta}(z)$ is defined as

$$s_{0\Delta}(z) = \begin{cases} 1 & \text{if } |z| < \frac{\Delta}{2} \\ \frac{1}{2} & \text{if } |z| = \frac{\Delta}{2} \\ 0 & \text{if } |z| > \frac{\Delta}{2} \end{cases}$$

Let $u(x, y)$ be a continuous function in $L^2(R)$ and let V_0 denote the space of functions which is spanned by piecewise continuous functions $s_{0\Delta}(x - \Delta k, y - \Delta l)$ where $(k, l) \in Z^2$. Let $\tilde{u}(x, y)$ be the projection of $u(x, y)$ on V_0 . Then we get

$$u(x, y) = \sum_{k=-\infty}^{\infty} \sum_{l=-\infty}^{\infty} u_0(k, l) s_{0\Delta}(x - \Delta k, y - \Delta l) \quad (3.2)$$

The samples $u_0(k, l)$ are given by

$$u_0(k, l) = \langle (u(x, y)), (s_{0\Delta}(x - \Delta k, y - \Delta l)) \rangle \quad (3.3)$$

where

$$\langle (u(x, y)), (s_{0\Delta}(x - \Delta k, y - \Delta l)) \rangle = \int_{-\infty}^{\infty} \int_{-\infty}^{\infty} u(x, y) s_{0\Delta}(x - \Delta k, y - \Delta l) dx dy \quad (3.4)$$

Let R denote the radon transform operator and let β denote the backprojection operator as discussed in chap 2. From the previous discussion the following relations hold

$$u_0(k, l) = u(x, y)|_{x=\Delta k, y=\Delta l} \quad (3.5)$$

$$\tilde{U}(\xi_1, \xi_2) = U(\xi_1, \xi_2) S_{0\Delta}(\xi_1, \xi_2) \quad (3.6)$$

Let F_{1d} denote one dimensional fourier transform operator and F_{1d}^{-1} denote the inverse fourier transform operator. We define some projections and their transforms as in eq 3.7 to eq 3.12. These relations are used in further discussion.

$$g(s, \theta) = Ru(x, y) \quad (3.7)$$

$$g(s, \theta) = R\tilde{u}(x, y) \quad (3.8)$$

$$w_{0\Delta}(s, \theta) = R s_{0\Delta}(x, y) \quad (3.9)$$

$$W_{0\Delta}(\xi, \theta) = F_{1d} w_{0\Delta}(s, \theta) \quad (3.10)$$

$$C(\xi, \theta) = F_{1d} g(s, \theta) \quad (3.11)$$

$$G(\xi, \theta) = F_{1d} \tilde{g}(s, \theta) \quad (3.12)$$

Using eq 3.6 to eq 3.12 we get

$$\tilde{G}(\xi, \theta) = G(\xi, \theta) W_{0\Delta}(\xi, \theta) \quad (3.13)$$

$$\begin{aligned} u_0(k, l) &= \beta(|\xi| W_{0\Delta}(\xi, \theta) C_u(\xi, \theta))|_{r=\Delta k, y=\Delta l} \\ &= \beta K(\xi, \theta) G_u(\xi, \theta) \end{aligned} \quad (3.14)$$

where

$$K(\xi, \theta) = |\xi| W_{0\Delta}(\xi, \theta) \quad (3.15)$$

Thus the filter $k(s, \theta) = I_{1d}^{-1} K(\xi, \theta)$ becomes the reconstruction filter in the convolution backprojection algorithm. The sampling kernel $s_{0\Delta}(x, y)$ along with its projection is shown in fig 3.1. As the sampling kernel $s_{0\Delta}(x, y)$ is separable in spatial domain, it is also separable in frequency domain, i.e.

$$W_{0\Delta}(\xi, \theta) = W_0(\xi \sin \theta) W_0(\xi \cos \theta) \quad (3.16)$$

where

$$W_0(\xi) = I_{1d} s_{0\Delta}(z) \quad (3.17)$$

It can be shown that

$$W_0(\xi) = \Delta \text{sinc}(\xi \Delta) \quad (3.18)$$

Hence we get

$$W_{0\Delta}(\xi, \theta) = \Delta^2 \text{sinc}(\Delta \xi \cos \theta) \text{sinc}(\Delta \xi \sin \theta) \quad (3.19)$$

$$K(\xi, \theta) = |\xi| \Delta^2 \text{sinc}(\Delta \xi \cos \theta) \text{sinc}(\Delta \xi \sin \theta) \quad (3.20)$$

The expressions for $k(s, \theta) = I_{1d}^{-1} K(\xi, \theta)$ are derived in appendix A. Using these results we get

$$k(s, \theta) = \frac{1}{\pi \sin 2\theta} \left(\ln \left| s^2 - \frac{\Delta^2}{4} (1 + \sin 2\theta) \right| - \ln \left| s^2 - \frac{\Delta^2}{4} (1 - \sin 2\theta) \right| \right), \theta \neq 0$$

$$k(s, 0) = -\frac{\frac{\Delta^2}{2}}{\pi \left(s^2 - \frac{\Delta^2}{4} \right)} \quad (3.21)$$

This is the expression for the reconstruction filter in the continuous case

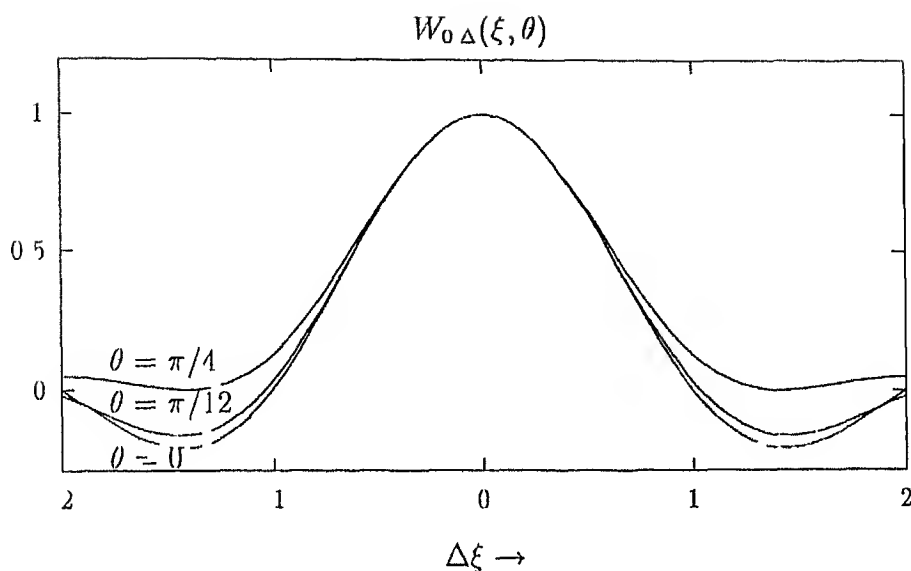


Figure 3.2 Plot of $W_{0\Delta}(\xi, \theta)$

3.2 Discrete Haar filter

The discrete haar filter $k_d(m, \theta)$ is obtained by sampling the continuous version. Looking at the plots of $W_{0\Delta}(\xi, \theta)$ (see fig 3.2) it is clear that if the sampling interval τ in projection domain is larger or even equal to Δ , strong aliasing will occur for all values of θ . The resulting artifacts degrade the reconstructed image considerably. Hence the projections are oversampled by a factor $\rho > 1$ and

$$\rho = \frac{\Delta}{\tau} \quad (3.22)$$

Also the function $k(s, \theta)$ described by eq 3.21 has some singularities at $(s = 0, \theta = \pi/4)$ and $(s = \Delta/4, \theta = 0.5 \arcsin(3/4))$. These singularities occur at sampled values of the trapezoidal shape where the derivatives are not defined. Hence the filter $k(s, \theta)$ is integrated by rectangular window and then sampled to obtain the discrete filter. Thus the projection is sampled at

$$s = n\tau = \frac{n\Delta}{\rho} \quad (3.23)$$

and

$$\begin{aligned}
k_t(n, \theta) &= \left(k(s, \theta) * \text{rect}\left(\frac{s}{\tau}\right) \right) = \\
&= \int_{(-\frac{1}{2})}^{(+\frac{1}{2})} k(u, \theta) du
\end{aligned} \tag{3.21}$$

The projections $w_{0\Delta}(s, \theta)$ need to be specified for $\theta \in [0, \pi/4]$. For other values of θ the following relations hold

$$w_{0\Delta}(s, \theta) = w_{0\Delta}(s, \pi/2 - \theta), \theta \in [\pi/4, \pi/2] \tag{3.25}$$

$$w_{0\Delta}(s, \theta) = w_{0\Delta}(s, \theta - \pi/2), \theta \in [\pi/2, 3\pi/4] \tag{3.26}$$

$$w_{0\Delta}(s, \theta) = w_{0\Delta}(s, \pi - \theta), \theta \in [3\pi/4, \pi] \tag{3.27}$$

Hence the function $W_{0\Delta}(\xi, \theta)$ follows the same symmetry. To evaluate the discrete filter we note that

$$\ln |s^2 - \tau^2| = \frac{d}{ds} [(s - \tau) \ln |s - \tau| + (\tau + s) \ln |\tau + s|] - 2 \tag{3.28}$$

Therefore integrating the above function we get

$$\begin{aligned}
k_t(n, \theta) &= \frac{1}{\pi \sin 2\theta} [(t - \alpha) \ln |t - \alpha| + (t + \alpha) \ln |t + \alpha| \\
&\quad - (t - \beta) \ln |t - \beta| - (t + \beta) \ln |t + \beta|]_{(-\frac{1}{2})}^{(+\frac{1}{2})} \tau, \quad \theta \neq 0
\end{aligned} \tag{3.29}$$

where

$$\alpha = \frac{\rho\tau}{2} \sqrt{1 + \sin 2\theta} = \frac{\rho\tau}{2} (\cos \theta + \sin \theta) \tag{3.30}$$

$$\beta = \frac{\rho\tau}{2} \sqrt{1 - \sin 2\theta} = \frac{\rho\tau}{2} (\cos \theta - \sin \theta) \tag{3.31}$$

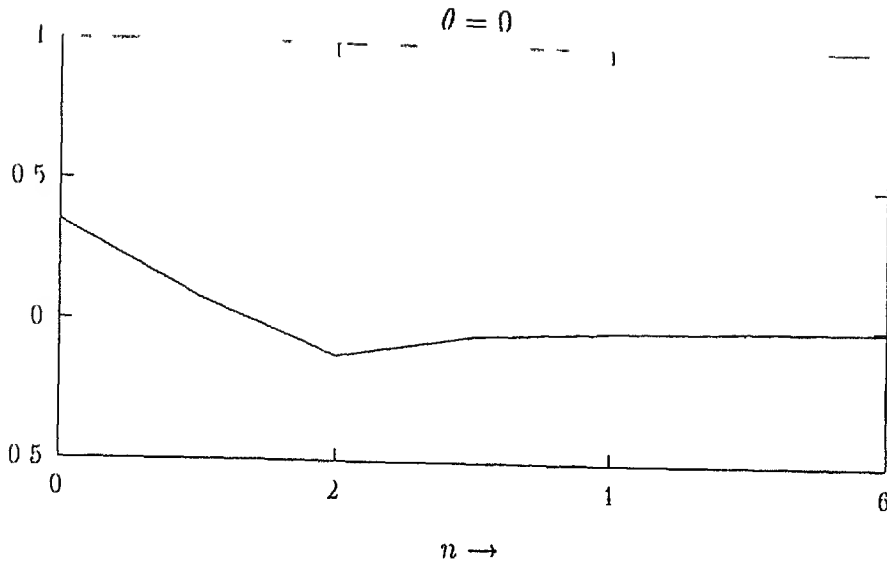


Figure 3.3 $k_d(n, 0)$ $\rho = 2$

The above expression for $k_d(n, \theta)$ is valid for $\theta \neq 0$. $k_d(n, 0)$ is similarly obtained by filtering and discretization of $k(s, 0)$. Thus

$$k_d(n, 0) = \frac{\Delta}{2\pi} \left(\ln \left| n^2 - \left(\frac{1+\rho}{2} \right)^2 \right| - \ln \left| n^2 - \left(\frac{1-\rho}{2} \right)^2 \right| \right) \quad (3.32)$$

The last equation clearly shows that the filter $k_d(n, 0)$ is still not defined for odd values of ρ which has singularities at $n = \pm(1+\rho)/2$ and $n = \pm(1-\rho)/2$. This is the major limitation of Haar filter.

The plots of $k_d(n, \theta)$ for various values of θ and ρ are shown in fig 3.3 to fig 3.10.

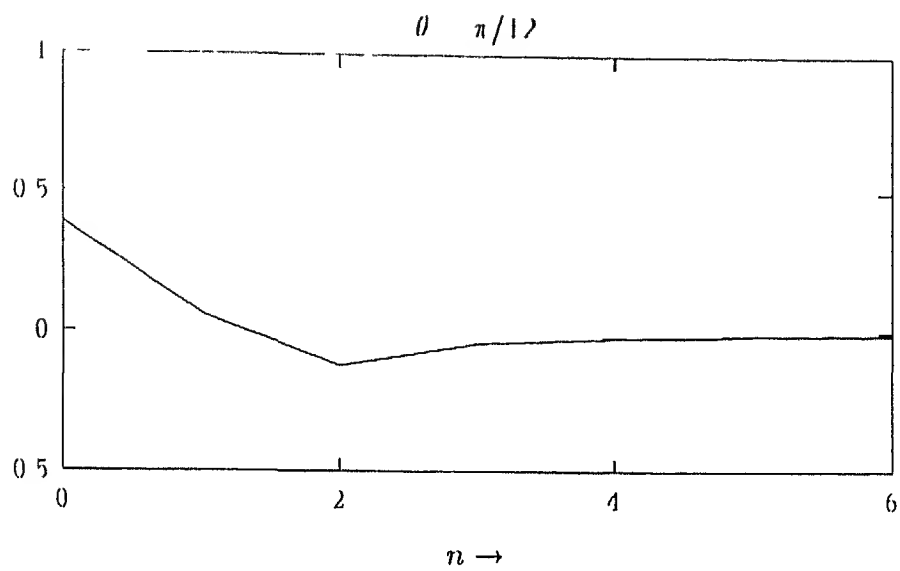


Figure 3.4 $k_l(n, \pi/12)$ $\rho = 2$

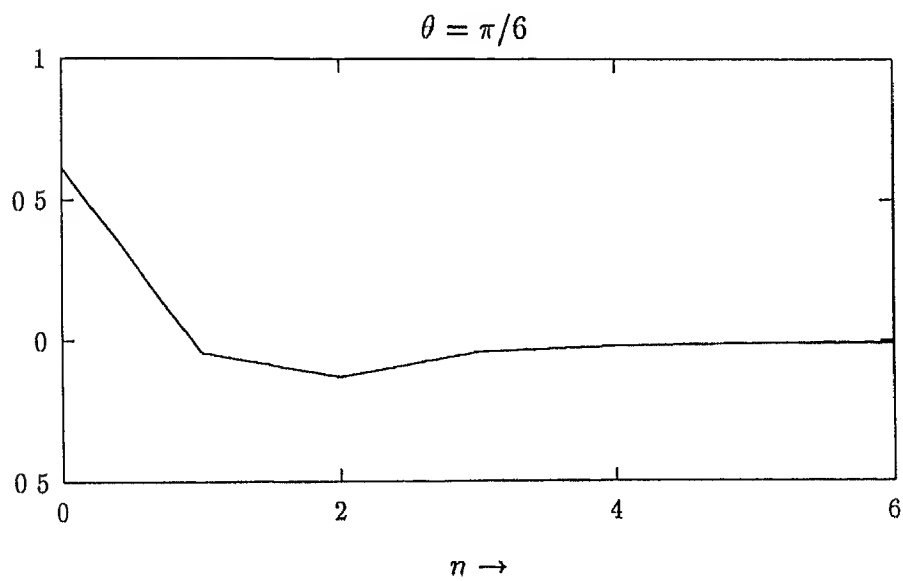


Figure 3.5 $k_d(n, \pi/6)$ $\rho = 2$

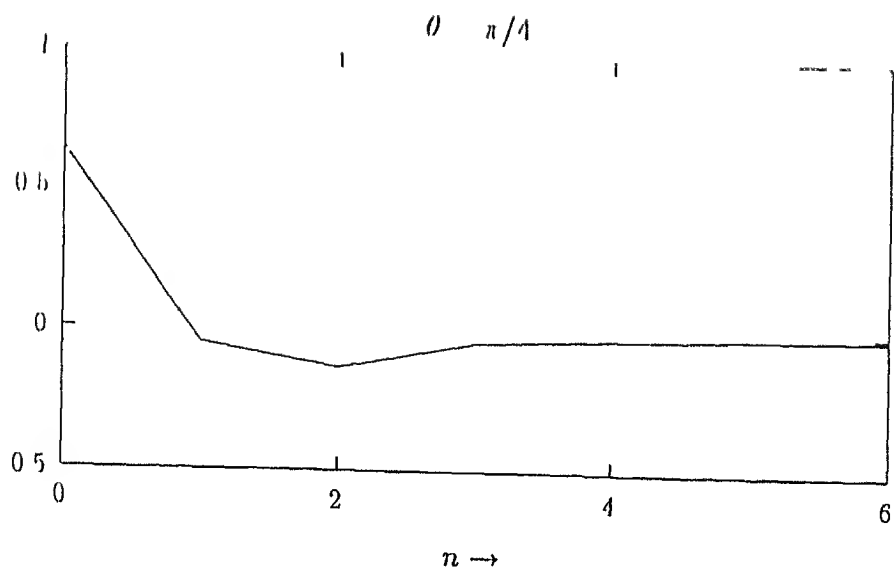


Figure 3.6 $k_d(n, \pi/4)$ $\rho = 2$

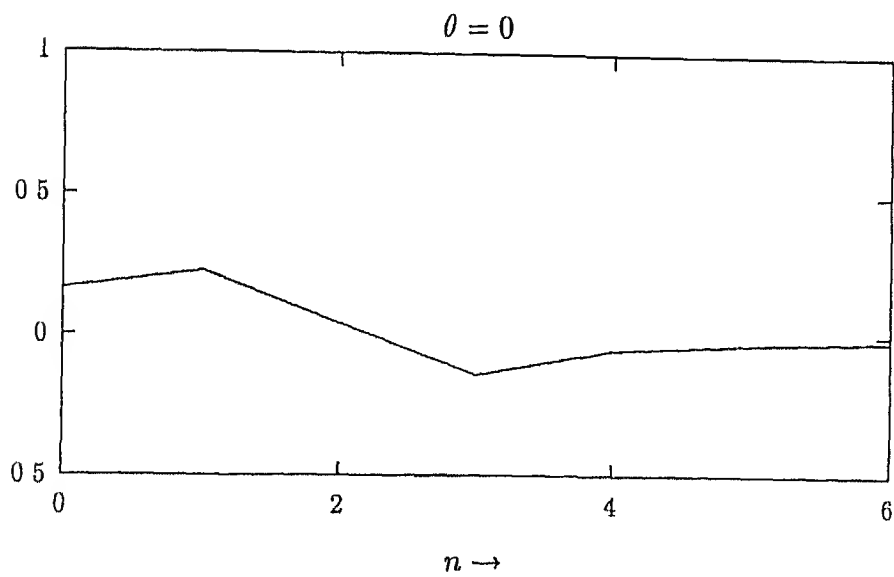


Figure 3.7 $k_l(n, 0)$ $\rho = 4$

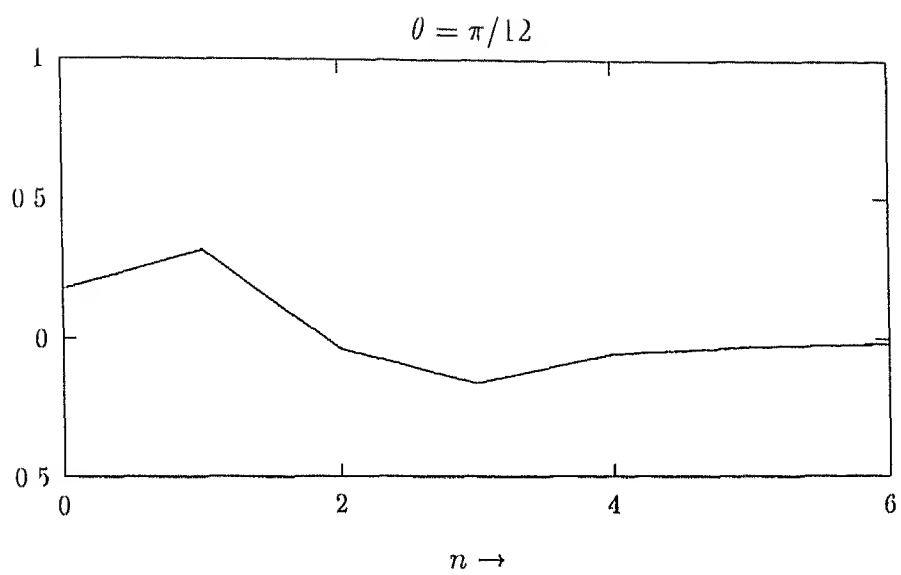


Figure 3.8 $k_l(n, \pi/12)$ $\rho = 4$

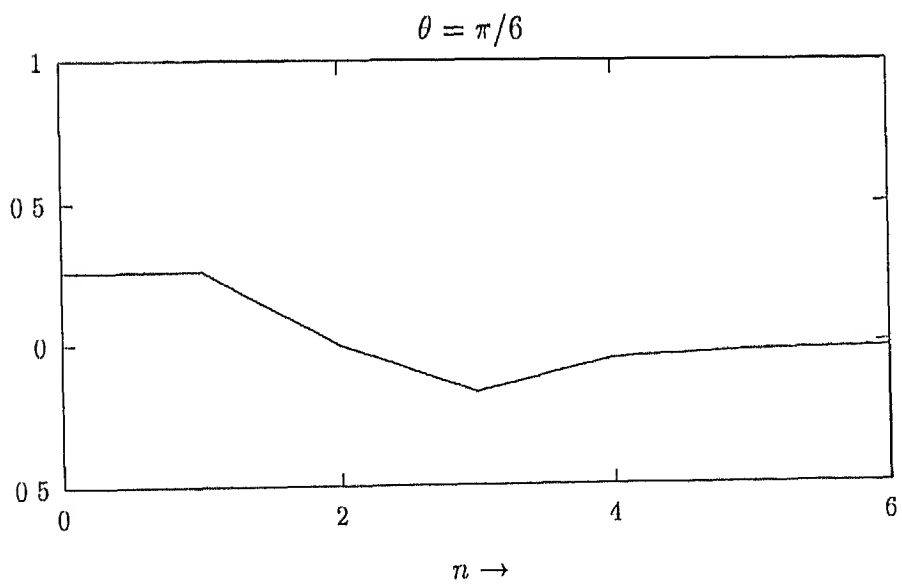


Figure 3.9 $k_d(n, \pi/6)$ $\rho = 4$

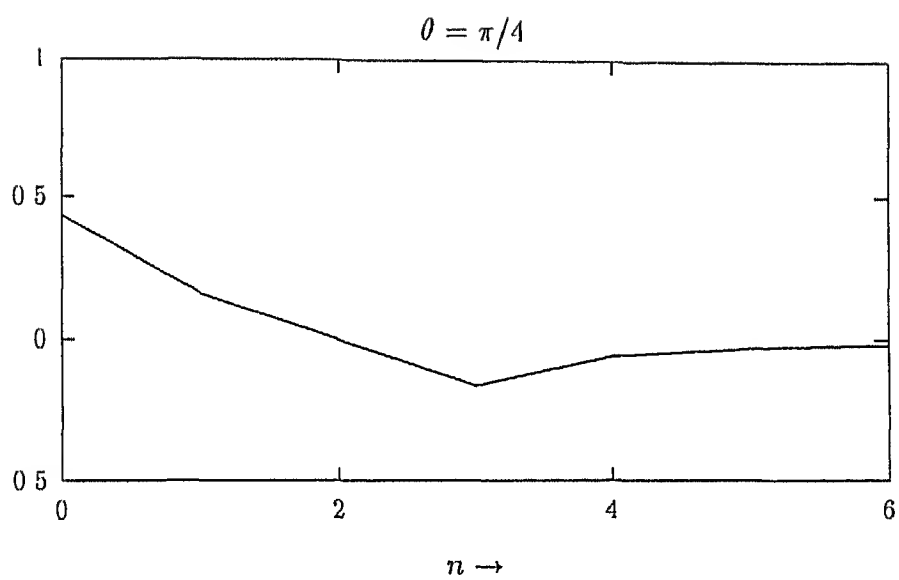


Figure 3.10 $k_d(n, \pi/4)$ $\rho = 4$

Chapter 4

Wavelet Transform

4.1 Introduction

For a one dimensional function $f(x)$ the fourier transform $F(\xi)$ is another representation of the same function specified in frequency domain. The fourier transform (and subsequently the inverse fourier transform) is orthogonal and all information in the original signal is preserved in the frequency domain. Note that we can write the inverse expression in the form

$$f(x) = \int_{-\infty}^{\infty} \langle f(x), e^{j2\pi\xi x} \rangle e^{j2\pi\xi x} d\xi \quad (4.1)$$

This indicates that the function $f(x)$ is expressed in terms of it's projections on the basis functions $e^{j2\pi\xi x}$. These functions are perfectly localized in frequency domain, but have infinite extent in time domain. Hence any time localized information in $f(x)$ such as abrupt changes, is spread in the whole spectrum. Hence the fourier transform lacks the knowledge about the time localized features of the signal. To address this problem, Gabouri introduced the window fourier transform, also called as 'short time fourier transform'(STFT), or Gabouri transform in 1946.

The STFT of a signal $f(t)$ is defined as

$$STFT_f(\xi, \tau) = \int_{-\infty}^{\infty} f(t)h(t - \tau)e^{-j2\pi\xi t} dt \quad (4.2)$$

where $h(t)$ is a low pass window like Gaussian window, which is localized in frequency domain as well as in time domain. The parameter ξ specifies the conventional frequency and τ specifies the time shift. Thus the transform $STFT_f(\xi, \tau)$ has significant magnitude only

if the signal $f(t)$ has significant spectral component of frequency ξ in the neighborhood of the time instant $t = \tau$. It is shown that to get fine frequency resolution, the window should be as wide as possible, and the condition of fine time resolution demands smaller support window. These conflicting requirements can not obviously be satisfied simultaneously and the Uncertainty Principle gives the lower limits on the product of the time scale resolution and frequency scale resolution [18]. The STFT uses a window of fixed support, hence of fixed bandwidth. This type of analysis is called uniform filter bank analysis [12].

In this regard the Wavelet transform offers the advantage over the other time frequency distributions. It allows one to have fine time scale resolution at the cost of frequency scale resolution and vice versa. (Within the limits imposed by the Uncertainty Principle, of course.) Along with Wavelets comes the notion of scale. The continuous parameter Wavelet transform is defined as

$$W_f(\tau, a) = \frac{1}{\sqrt{a}} \int_{-\infty}^{\infty} f(x) \psi\left(\frac{x - \tau}{a}\right) dx \quad (4.3)$$

The window function $\psi(x)$, called as mother Wavelet, is a bandpass function. In Wavelet transform, the analyzing window is scaled (ie either dilated or contracted) and the shifting parameter τ is made a function of the scale parameter a . Thus narrow windows are shifted by small interval and wider windows shifted by large intervals. This results in 'constant Q' filter bank analysis [12]. The Wavelet transform given by eq 4.3 is invertible provided the mother wavelet satisfies the admissibility condition [18] given as

$$\int_{-\infty}^{\infty} \frac{|\Psi(\xi)|^2}{|\xi|} d\xi = 1 \quad (4.4)$$

where

$$\Psi(\xi) = \int_{-\infty}^{\infty} \psi(x) e^{-j2\pi\xi x} dx \quad (4.5)$$

When $\psi(x)$ is having fast decay at infinity [18], the admissibility condition can also be written as

$$\int_{-\infty}^{\infty} \psi(x) dx = 0 \quad (4.6)$$

This indicates that $\psi(x)$ is oscillatory.

4.2 Discrete Parameter Wavelet Transform

The Wavelet transform given by eq 4.3 is very much redundant. The same is true for the STFT also. Hence it is desirable to discretize the parameters (a, τ) ((ξ, τ) in case of

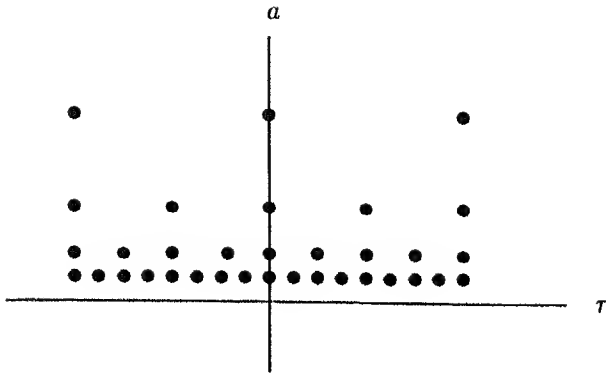


FIGURE 4.1 Dyadic grid for discretization of (a, τ)

SIFT) In fact we would like to have a specific grid for (a, τ) such that the associated wavelets $\{\psi_{a, \tau}(t)\}$ are orthogonal where

$$\psi_{a, \tau}(x) = \frac{1}{\sqrt{a}} \psi\left(\frac{x - \tau}{a}\right) \quad (4.7)$$

The orthogonality implies no redundancy. It is shown that for SIFT, when the sampling grid is selected so as to achieve the orthogonality, the corresponding window functions are very badly localized either in time domain or in frequency domain [15]. This is why most of the time the SIFT is oversampled. However for Wavelet transform, it is possible to achieve orthogonality along with localization [15]. The discrete parameter Wavelet transform is defined as

$$\begin{aligned} DWT_f(m, n) &= W_f(a_0^m, nb_0 a_0^m) \\ &= a_0^{-\frac{n}{2}} \int_{-\infty}^{\infty} f(x) \psi(a_0^{-m} x - nb_0) dx \end{aligned} \quad (4.8)$$

Meyer has shown that there exist a class of wavelets $\{\psi(\tau)\}$ for which the choice $a_0 = 2$ and $b_0 = 1$ gives orthogonal bases of $L^2(\mathbb{R})$. This corresponds to the dyadic grid as shown in fig 4.1

4.3 Wavelets and Multiresolution Analysis

The multiresolution analysis methods are widely used in computer vision for the purpose of pattern recognition. In this section we will consider in brief the relation between

multiresolution analysis and wavelet transform. A more detailed treatment can be found in [12].

The multiresolution analysis consists in breaking up $L^2(R)$ into a ladder of spaces V_j

$$\dots \subset V_2 \subset V_1 \subset V_0 \subset V_{-1} \subset V_{-2} \dots \quad (4.9)$$

The orthogonal projection of some function $f(x) \in L^2(R)$ on V_j corresponds to approximation of $f(x)$ at resolution 2^j . The Multiresolution approximation has following properties

- $f(x) \in V_j \Rightarrow f(2^j x) \in V_0$
- There exists a scaling function $\phi(x)$ such that $\{\phi_{0,n}(x)\}_{n \in \mathbb{Z}}$ is orthogonal basis of V_0 where $\phi_{0,n}(x) = \phi(x-n)$. This also implies that $\{\phi_{j,n}(x) = 2^{-\frac{j}{2}} \phi(2^{-j}x - n)\}_{n \in \mathbb{Z}}$ forms the bases of V_j . Note that the factor $2^{-\frac{j}{2}}$ is present so as to make the $L^2(R)$ norms of $\phi(x)$ and $\phi_{j,n}(x)$ identical.
- Let us define the orthogonal complement of V_j in V_{j+1} by W_j , i.e. $V_{j+1} = V_j \oplus W_j$. Then there exists a function $\psi(x)$ such that $\{\psi_{j,n}(x)\}$ is orthogonal bases of W_j , where

$$\psi_{j,n}(x) = 2^{-\frac{j+1}{2}} \psi(2^{-j}x - n) \quad (4.10)$$

- Let A_j denote the orthogonal projection operator on V_j . We denote the projection of $f(x)$ on V_j by $A_j f(x)$. Then $A_j f(x)$ is completely characterized by the sequence $\{\alpha_{j,n}\}$ where

$$\alpha_{j,n} = \langle f(x), \phi_{j,n}(x) \rangle \quad (4.11)$$

- The approximation at a resolution level j is coarse approximation as compared to approximation at resolution level $j+1$. The resulting loss of information is given by orthogonal projection of $f(x)$ on W_j and is called as detail signal at a resolution level j . Let D_j denote the orthogonal projection operator on the subspace W_j . Then $D_j f(x)$ is completely characterized by the sequence $\{d_{j,n}\}$ where

$$d_{j,n} = \langle f(x), \psi_{j,n}(x) \rangle \quad (4.12)$$

- The functions $\phi_{j,n}(x)$ & $\psi_{j,n}(x)$ satisfy the following relations

$$\langle \phi_{j,k}(x), \phi_{j,m}(x) \rangle = \delta_{k-m}$$

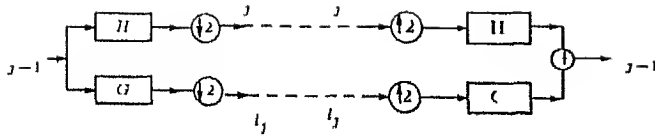


Figure 4.2 2 channel perfect reconstruction quadrature mirror filter bank

$$\langle \psi_{j,k}(x) | \phi_l(\tau) \rangle = \delta_{j-l} \delta_{k-n} \quad (4.13)$$

From the foregoing discussion it is clear that $\{\psi_{j,n}\}, (n,j) \in \mathbb{Z}^2$ is orthogonal basis of $L^2(\mathbb{R})$. Mallat has shown [12] how to obtain the sequence $\{\alpha_{j,n}\}$ and $\{d_{j,n}\}$ given the sequence $\{\alpha_{j-1,n}\}$ and vice versa. This scheme is shown in fig 4.2

These sections are identical with the analysis and synthesis sections of 2 channel ,perfect reconstruction quadrature mirror filter bank (QMF)[19]. The filters, G , & H satisfy the conditions

$$|H(\omega)|^2 + |H(\omega + \pi)|^2 = 1 \quad (4.14)$$

$$H(z)G(z^{-1}) + H(-z)G(-z^{-1}) = 0 \quad (4.15)$$

where

$$H(z) = \sum_{n \in \mathbb{Z}} h(n) z^{-n} \quad (4.16)$$

$$G(z) = \sum_{n \in \mathbb{Z}} g(n) z^{-n} \quad (4.17)$$

$$G(\omega) = G(z)|_{z=e^{j\omega}} \quad (4.18)$$

$$H(\omega) = H(z)|_{z=e^{j\omega}} \quad (4.19)$$

The concept of multiresolution resolution can be extended to 2D images [13]

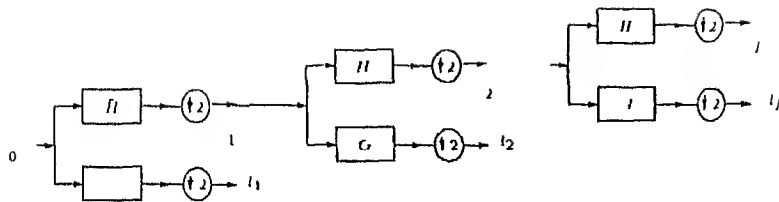


Figure 4.3 Pyramid algorithm Analysis section

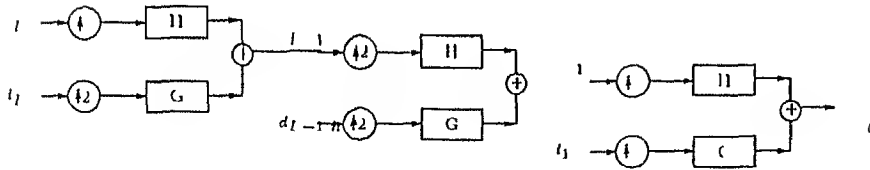


Figure 4.4 Pyramid algorithm Synthesis section

4.4 Fast Wavelet Transform

In practice the signal $f(t)$ is sampled with finite sampling rate $1/T$, to obtain the sequence $\{u(n)\}$ $u(n) = f(nT)$. These samples can be supposed to give projection of $f(t)$ on ψ_0 or $\alpha_0 n = u(n)$. The wavelet coefficients $d_{j,k}$ $I \geq j \geq 1$ can be obtained using the pyramid algorithm as shown in fig 4.3. The synthesis scheme is shown in fig 4.4. This is the fast wavelet transform algorithm.

4.5 Compactly supported orthonormal basis

Using the concepts developed by Mallat, Daubechies has shown how to obtain compactly supported wavelet bases from the quadrature mirror filters [20]. The Daubechies wavelets have finite region of support. The length of the filter $h(n)$ varies accordingly. The plots of wavelets and scaling functions for different filter lengths are shown in fig 4.5 to fig 4.5. The filter coefficients are given in [15]. Filters of length 4 & 8 are considered for demonstration.

The orthogonal wavelets and scaling functions in general are not symmetric. This results in nonlinear phase filters in analysis and synthesis filter banks. By adopting bi-orthogonal filters, the condition of linear phase can be satisfied. However this is at the cost of using separate scaling function and wavelet in analysis and synthesis sections of the multiresolution decomposition. For additional details the reader is referred to [17].

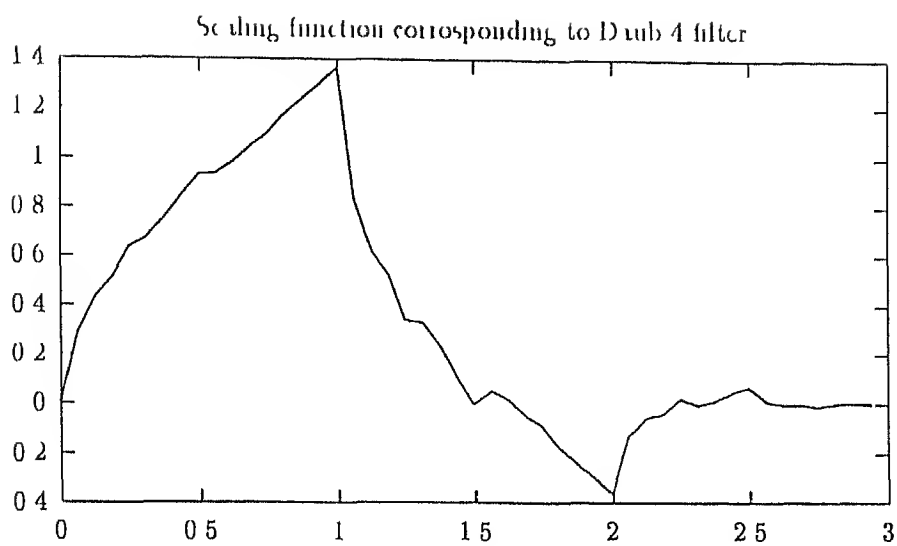


Figure 4.5 Scaling function for Daub 4 filter

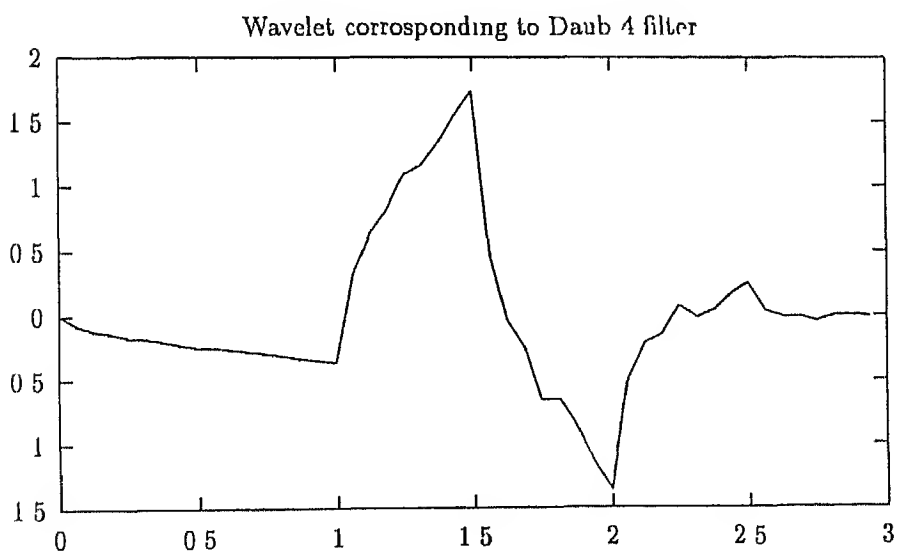


Figure 4.6 Wavelet for Daub 4 filter

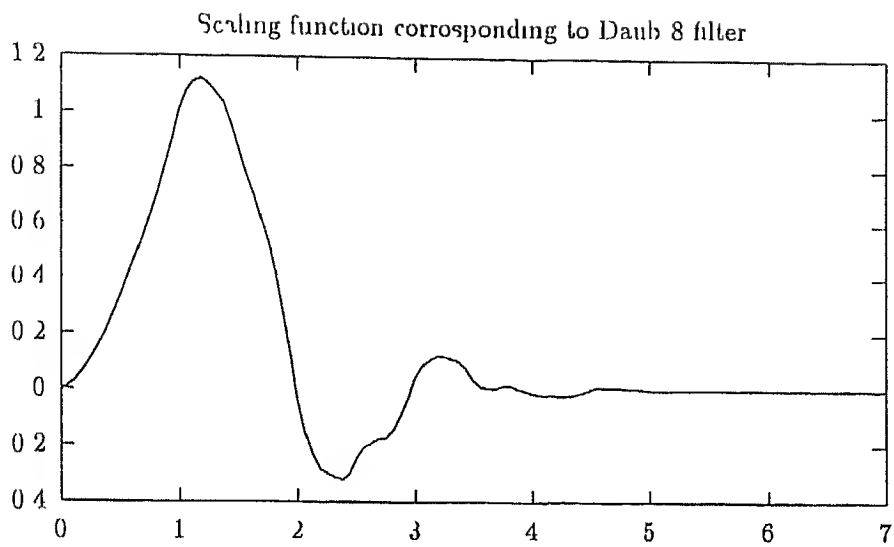


Figure 4.7 Scaling function for Daub 8 filter

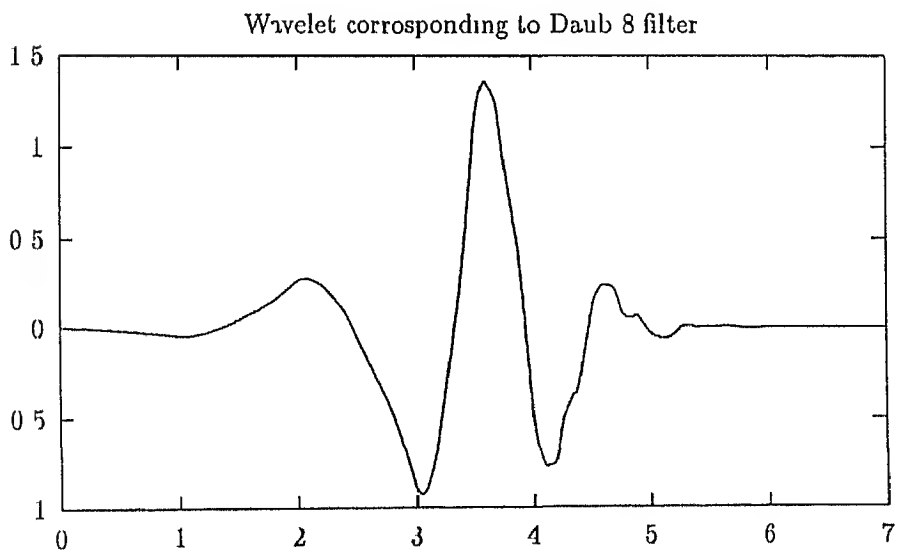


Figure 4.8 Wavelet for Daub 8 filter

Chapter 5

Wavelets in Tomography

5.1 Review

As mentioned in the first chapter, the time-frequency localization property of wavelet transform is utilized in the applications like region of interest tomography [5], space variant noise filtering [9], [10] etc. In region of interest tomography, only a small cross sectional area is reconstructed at a higher resolution. Using wavelet expansion of the image, this reconstruction can be carried out using less no. of samples per projection [5], with a subsequent reduction in X-ray dosage. Another application of wavelet transform is the spatially varying filters for noise suppression. Once again the space-frequency localization property of wavelet transform is made use of. In this chapter this application is considered in more details.

5.2 Space varying filtering

The projections sampled in the tomography are normally corrupted with noise. The statistical nature of photon emission is the main source of noise [2]. This noise can be modeled as additive white gaussian noise with zero mean [11]. Thus we get

$$g_r(s, \theta) = g_u(s, \theta) + \mu(s, \theta) \quad (5.1)$$

where $g_r(s, \theta)$ is the corrupted projection data, $g_u(s, \theta) = Ru(x, y)$ and $w(s, \theta)$ is the additive white gaussian noise with zero mean and variance σ^2 . The noise component is uncorrelated in both the variables s and θ . Thus using the expectation operator [22] we get

$$I [\mu(s_1, \theta_1) \mu(s_2, \theta_2)] = \sigma^2 \delta_{s_1} \delta_{\theta_1, \theta_2} \quad (5.2)$$

Using the sampled versions we get

$$g_n^r(m) = g_n^u(m) + \mu_n(m) \quad (5.3)$$

For the sake of simplicity we will drop the term n as the foregoing discussion is equally applicable to all the projection angles.

Let d_j^r , d_j^u and d_j^l denote the discrete wavelet transform coefficients of noisy projections, uncorrupted projections and white noise component respectively, at resolution level j . Using the linearity property of the wavelet transform we get

$$d_j = d_j^u + d_j^l \quad (5.4)$$

For reduction of noise power, the projections can be low pass filtered using linear filters. This however, results in loss of spatial resolution. The solution proposed to this problem [5] is a space variant filter in which, only those wavelet coefficients, which have magnitude below a certain threshold, are set to zero. As the wavelet coefficients represents the detail signal or high frequency components, this is equivalent to space variant low pass filtering. The processed wavelet coefficients $\tilde{d}_{i,j}$ are thus given by

$$d_{i,j} = \begin{cases} d_{i,j}^r & \text{if } |d_{i,j}^r| > \lambda(i) \\ 0 & \text{if } |d_{i,j}^r| < \lambda(i) \end{cases} \quad (5.5)$$

where $\lambda(i)$ is some threshold corresponding to level i .

5.3 Selecting the threshold

For threshold selection we use the energy criteria given in [24],[23]

The threshold $\lambda(i)$ is selected such that the total energy of the processed detail signal at resolution level i is close to the total energy of the wavelet coefficients d_j^u (which corresponds to uncorrupted projections) at the same resolution level. For orthogonal wavelet representation we have

$$P^r = \sum_j (d_{i,j})^2 \quad (5.6)$$

where P_i^r is the total energy of the detail coefficients of the received data at a resolution level i .

Expanding above equation we get

$$P^r = \sum_j (d_{i,j}^u + d_{i,j}^l)^2 \quad (5.7)$$

$$= \sum_j (d_{i,j}^u)^2 + \sum_j (d_{i,j}^l)^2 + 2 \sum_j d_{i,j}^u d_{i,j}^l \quad (5.8)$$

Note that the white noise is assumed to be uncorrelated with $g(s, \theta)$ and is also assumed to be of zero mean and variance σ^2 . Hence we get

$$E[d_{i,j}^u d_{i,j}^l] = 0, \forall i, \forall j \quad (5.9)$$

$$E[(d_{i,j}^l)^2] = \sigma^2 \quad (5.10)$$

$$(5.11)$$

Here E denotes the expectation operator and it can be shown that [22],[24]

$$\sigma_i^2 = \sigma^2 (\sum_n g(n)^2) (\sum_n h(n)^2)^{i-1} \quad (5.12)$$

Hence from eq 5.8 & 5.11 we get

$$L[P_i^r] = P_i^u + L[P_i^l] \quad (5.13)$$

where

$$\begin{aligned}
I[P'] &= I[\sum_j (d''_j)^2] \\
&= \sum_j I[(d''_j)^2] \\
&= \sum_j \sigma^2
\end{aligned} \tag{11}$$

Let M denote the total no of samples per projection. As there is a decimation by a factor of two after every filtering stage of the analysis section (see fig 4.3) it follows that if M is the no of wavelet coefficients at resolution level i then $M = M2^{-i}$ and

$$\begin{aligned}
I[P''] &= \sum_j^{M-1} \sigma^2 \\
&= M2^{-i} \sigma_1^2
\end{aligned} \tag{15}$$

The threshold $\lambda(i)$ is selected such that all the wavelet coefficients (at a resolution level i), whose magnitude is below the threshold have a total energy approximately equal to $I[P'_i]$. The processed wavelet coefficients are then inverse transformed and the processed projections are used for image reconstruction.

This technique has already been used successfully for noise filtering and is shown to give better performance compared to linear space invariant filters [23-9]. The objective of using this method here is to see the combined effect of Harr filter and wavelet pre processing. The results of computer simulation are given in next chapter.

Chapter 6

Simulation results

6.1 Standard Reconstructions

In this chapter we present the results of computer simulation to demonstrate the effectiveness of the Hsu filter. In the first section we consider the reconstruction of a square image. The square image is defined as

$$u(x, y) = \begin{cases} 1 & \text{if } |x| < 0.5, |y| < 0.5 \\ 0 & \text{otherwise} \end{cases} \quad (6.1)$$

The projections of the square have a trapezoidal shape as discussed in appendix A and can be calculated in a straightforward manner. The projections are sampled so as to get 200 samples per projection, ie $M = 200$ and no of projection angles $N = 128$. The square image is reconstructed on a grid of 100×100 . This gives a oversampling ratio $\rho = 2$. The reconstruction is carried out without adding any noise to the projections. Different convolvers are used for comparison purpose. Similarly, using 400 samples per projections, which gives oversampling ratio $\rho = 4$, reconstruction is carried out. The reconstructed image is normalized so as to get a value of 1.0 at the center pixel.

We compare the performance of different convolvers. Let $u(k, l)$ denote the reconstructed image after normalization. We define the Signal to Noise ratio SNR as

$$SNR = 10 \ln \frac{\sum_k \sum_l [u(k, l)]^2}{\sum_k \sum_l [u(k, l) - \tilde{u}(k, l)]^2} \quad (6.2)$$

The results are presented in table 6.1

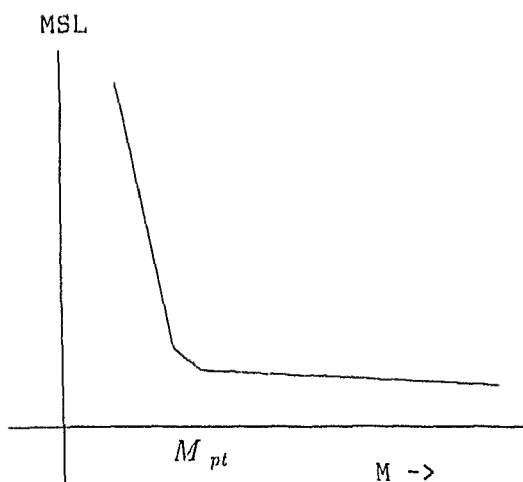


Figure 6.1 MSL Vs M with constant N

This table shows that for Haar filter the SNR improves with increasing value of p while for other filters the performance deteriorates and the SNR falls. This results however does not match with the error curve given in [25]. The curve is reproduced here in fig 6.1. Thus the Mean Square Error is shown to saturate to a minimum value after M exceeds an optimum value given by $M = 2 * N/\pi$. We feel that this discrepancy could be due to increased quantization, computation and rounding noise which increases with increased bandwidth. Also with increased bandwidth the reconstructed square has higher overshoot and undershoot along the edges. However for Haar filter the reconstruction filter is a function of oversampling ratio p and it takes into account the increased projection bandwidth.

Note that the Ram Lak filter has ramp like response with sharp cutoff. This results in sharp transition of the square edges with high overshoot and ringing. The overshoot and ringing can be reduced by having a smooth roll off as in case of Generalized Hanning filter. However this is at the cost of wider transition width. The parameter α of the G-H filter allows a tradeoff between overshoot and transition width. $\alpha = 1$ corresponds to Ram Lak filter. For comparison purpose we have selected a center value of 0.5. The cross section of the reconstructed square is displayed in fig 6.2(a). The bottom and top corners of the transition region are expanded and displayed in fig 6.2(b) and 6.2(c) respectively. The figure shows that Ram Lak has smallest transition width but have high overshoot. The transition width of Haar filter is comparable to that of Shepp Logan filter with smaller overshoot.

Filter	$\rho = 2$	$\rho = 3$	$\rho = 4$
Run Ink	26.35	23.04	20.74
Shepp Logan	28.81	25.62	23.20
Generalized Hamming	30.07	26.92	24.33
Hu	35.58	—	37.05

Table 6.1 Performance comparison (No noise added)

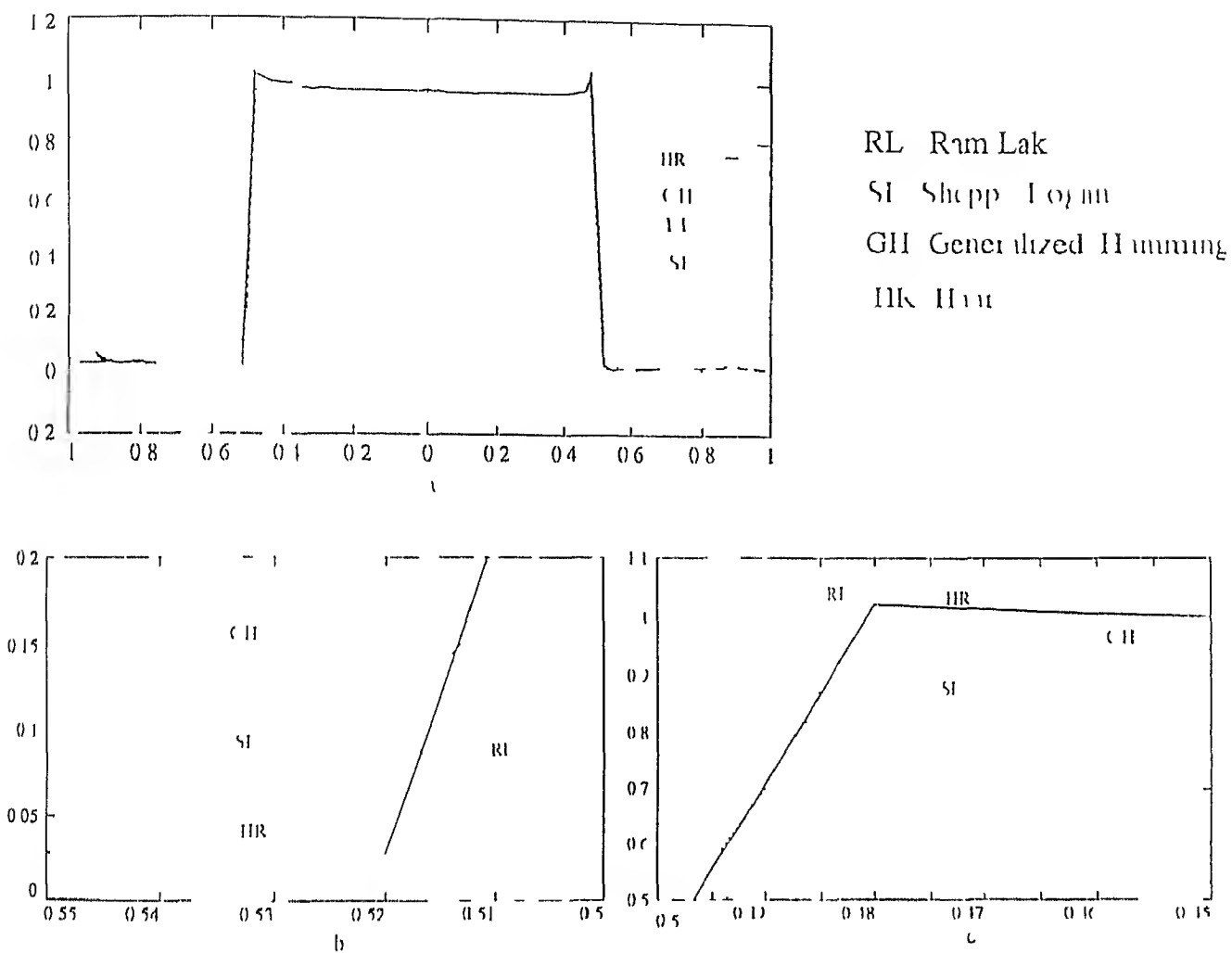


Figure 6.2 Cross sectional view along edge

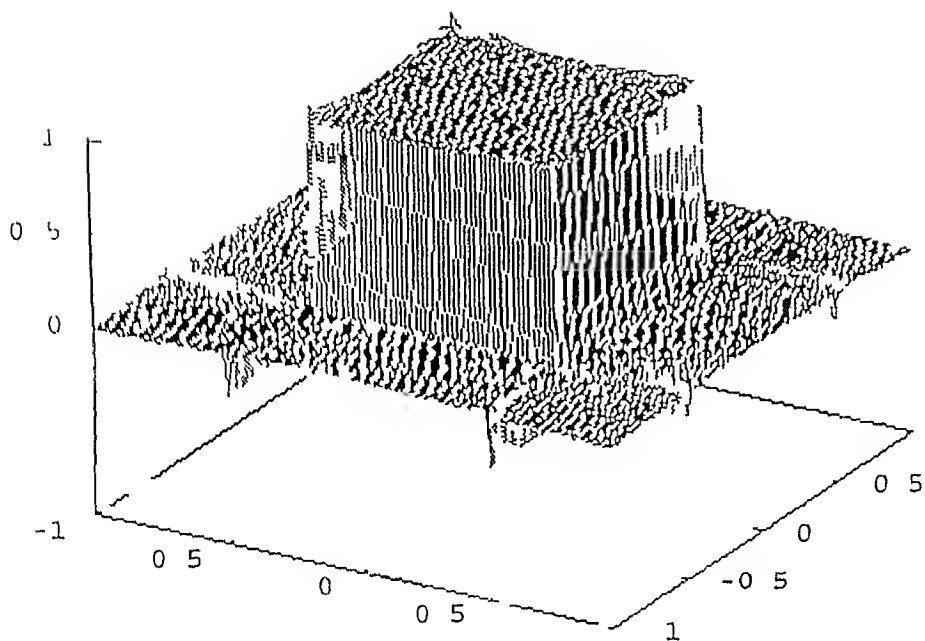


Figure 6.3 Square reconstruction using Runge-Kutta filter $\rho = 2$

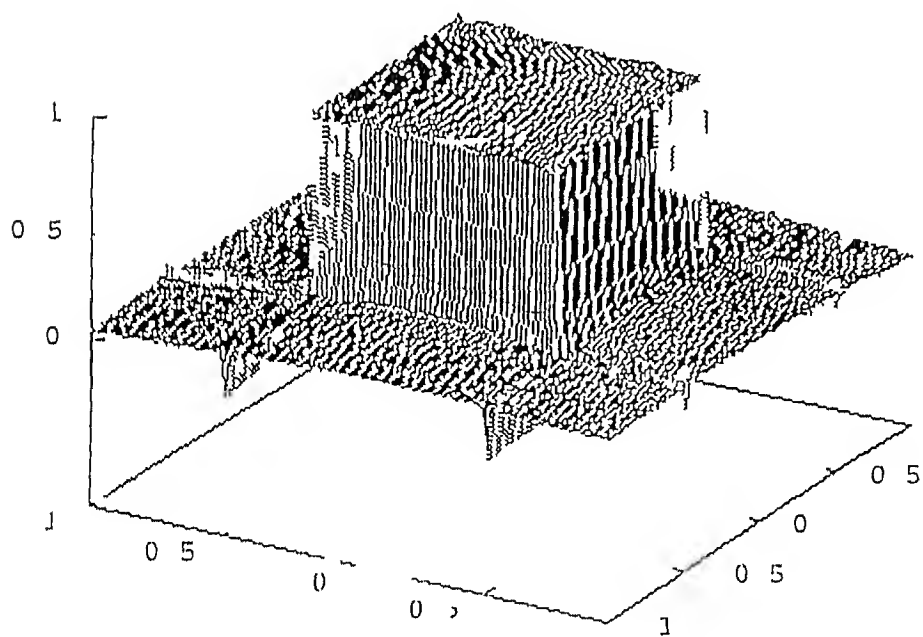


Figure 6.4 Square reconstruction using Shepp-Logan filter $\rho = 2$

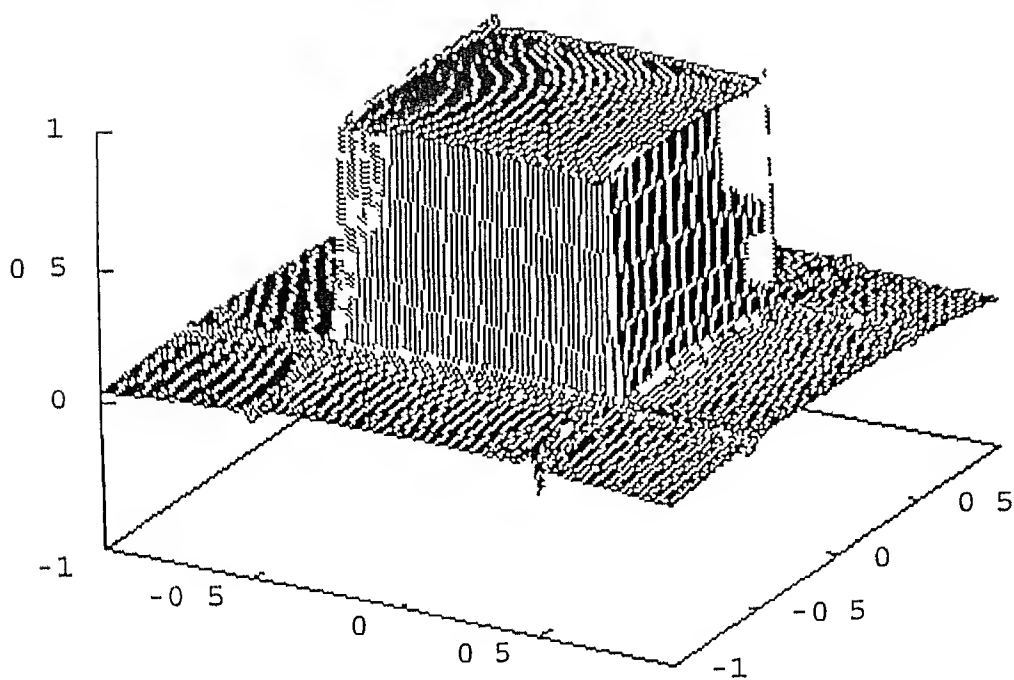


Figure 6.5 Square reconstruction using Generalized Hamming filter $\rho = 2$

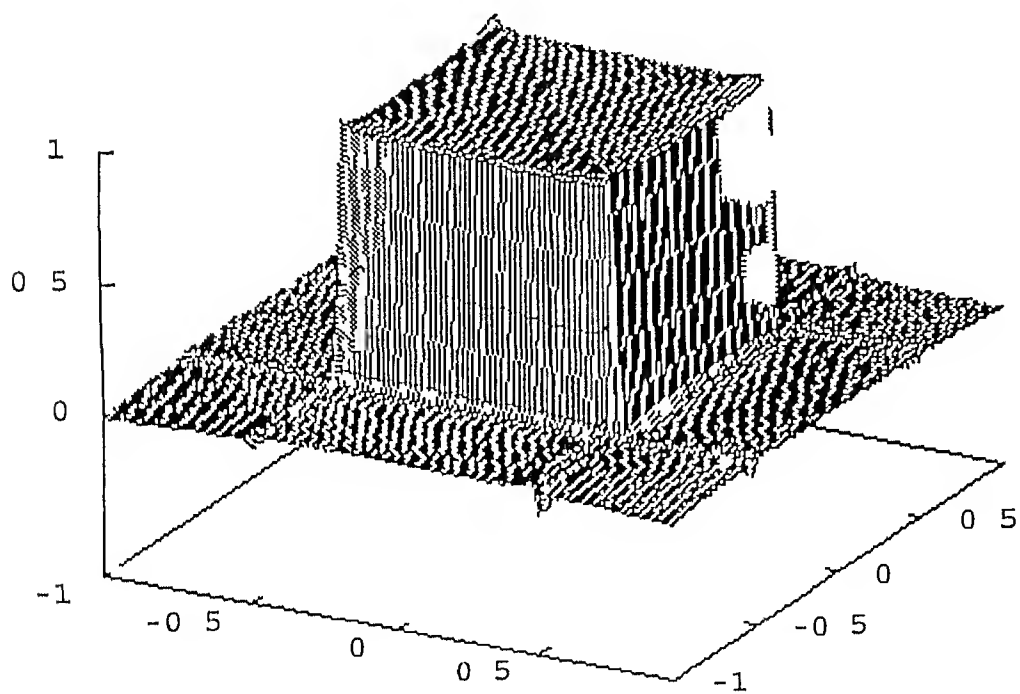


Figure 6.6 Square reconstruction using Haar filter $\rho = 2$

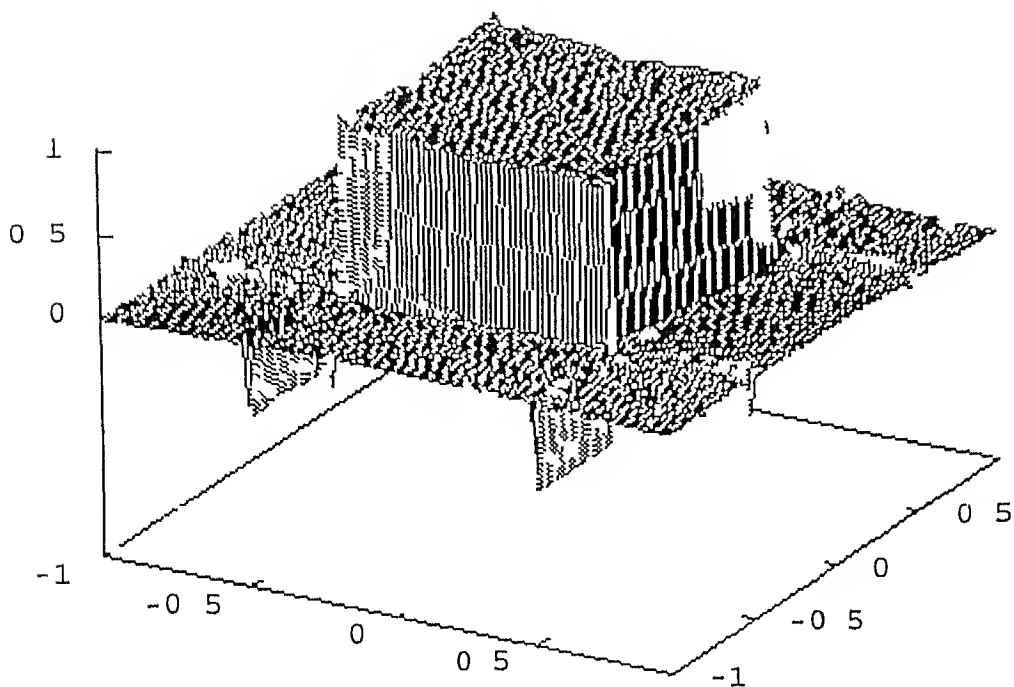


Figure 6.7 Square reconstruction using Ram Lak filter $\rho = 4$

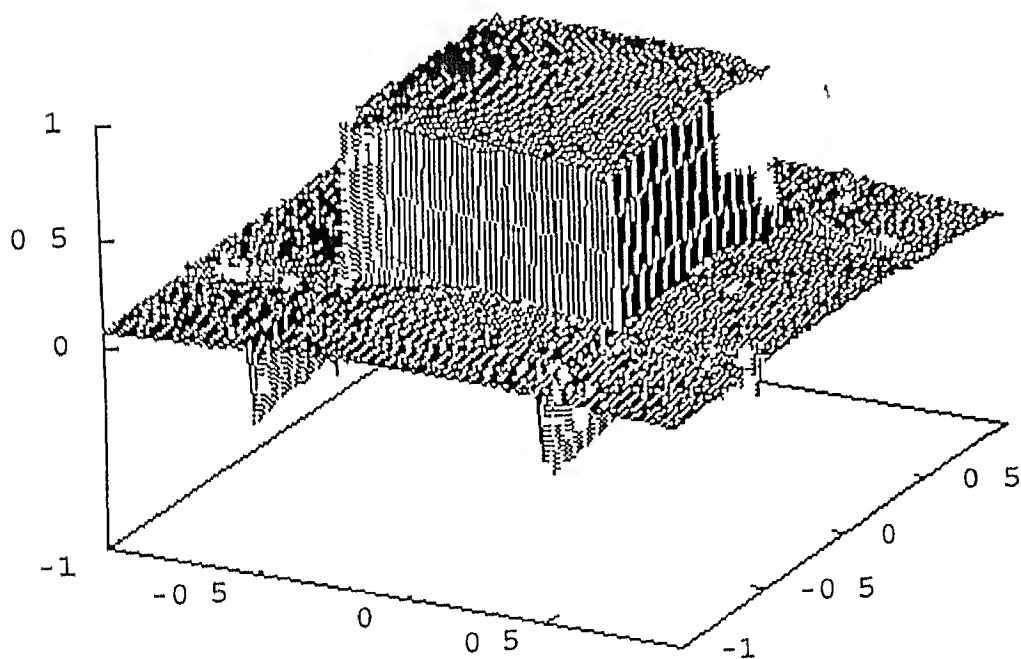


Figure 6.8 Square reconstruction using Shepp Logan filter $\rho = 4$

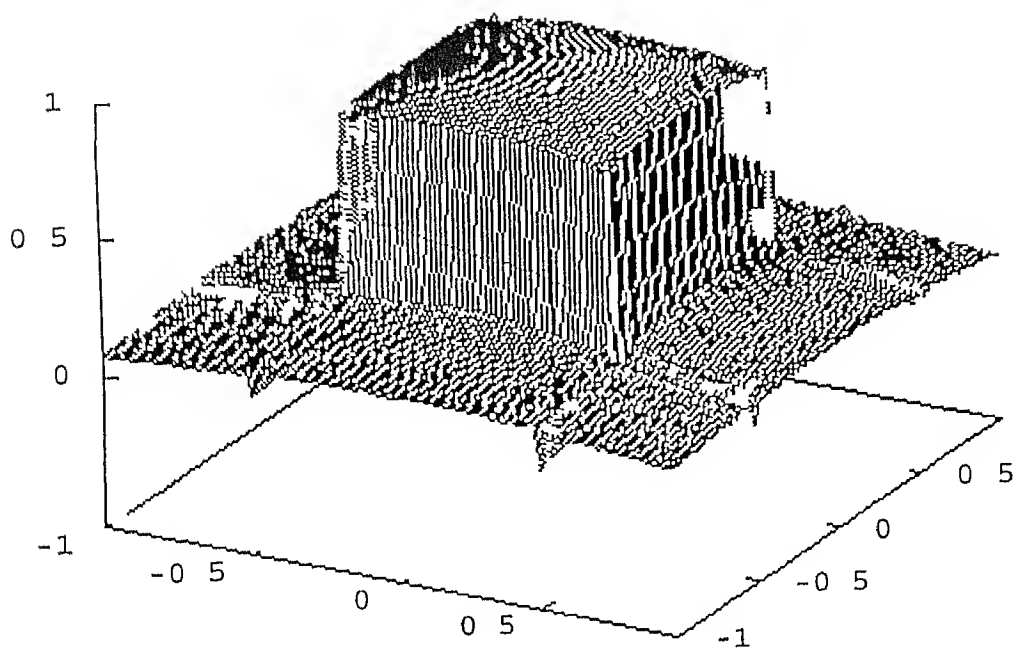


Figure 6.9 Square reconstruction using Generalized Hamming filter $\rho = 4$

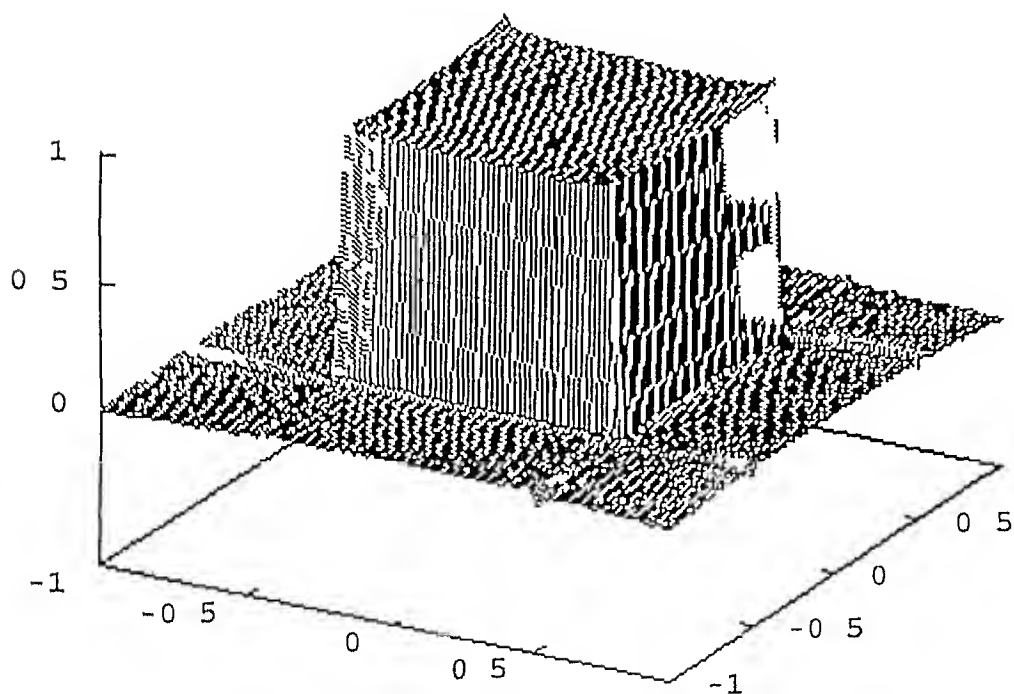


Figure 6.10 Square reconstruction using Haar filter $\rho = 4$

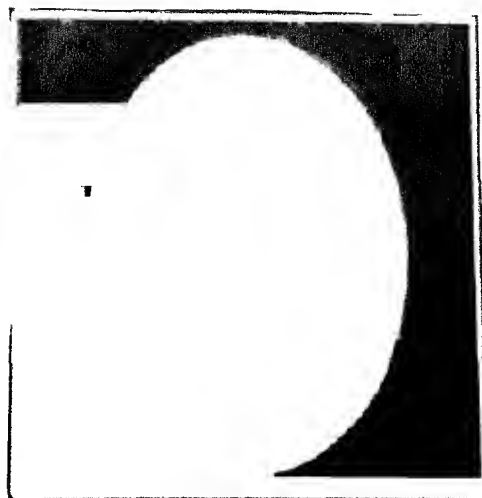


Figure 6 11 Phantom reconstruction using Generalized Hamming filter $\rho = 4$



Figure 6 12 Phantom reconstruction using Haa1 filter $\rho = 4$

6 2 Reconstruction from Noisy projections

Now we consider the reconstruction from noisy projections using wavelet preprocessing. The filter used for wavelet decomposition is Daubechies 8. (The simulation was also carried out with filters of length 4,10,and 20. However there was not significant change in performance.)

The value of SNR is evaluated for different convolvers at different oversampling ratio ρ and different noise powers. Two cases are considered separately. In first case white gaussian noise of zero mean is added to the projections. No wavelet pre processing is carried and the SNR is measured for different noise powers. These results are summarized in table 6 2 and 6 4. In the second case, pre processing of noisy projections, as discussed in chp5 is carried out before convolution and backprojection. The results are summarized in table 6 3. The same procedure is repeated for $\rho = 2$ and the results are presented in table 6 3 and 6 5. In all these cases, the normalization factor used is same as in case of noiseless reconstruction with respective filters and oversampling ratio.

Filter	$\sigma_\mu^2 = 0.001$	$\sigma_\mu^2 = 0.0005$	$\sigma_\mu^2 = 0.0001$
Ram Lak	8.69	13.72	18.94
Shepp Logan	11.04	14.58	21.09
Generalized Hamming	20.51	21.72	22.843
Haar	31.69	34.03	36.90

Table 6 2 Performance comparison at various noise powers. No pre processing $\rho = 4$

Filter	$\sigma_\mu^2 = 0.001$	$\sigma_\mu^2 = 0.0005$	$\sigma_\mu^2 = 0.0001$
Ram Lak	19.75	20.04	20.51
Shepp Logan	21.67	22.73	23.98
Generalized Hamming	23.01	23.02	23.12
Haar	36.02	36.39	36.38

Table 6 3 Performance comparison at various noise powers, with wavelet pre processing $\rho = 4$

Filter	$\sigma_t^2 = 0.001$	$\sigma_t^2 = 0.0005$	$\sigma_t^2 = 0.0001$
Run 1 uk	19.74	22.36	25.35
Shepp Logan	20.46	24.40	28.65
Generalized Hamming	27.11	29.03	28.67
Hu	31.18	33.170	35.08

Table 6.4 Performance comparison at various noise powers with no pre processing $\rho = 2$

Filter	$\sigma_t^2 = 0.001$	$\sigma_\mu^2 = 0.0005$	$\sigma_t^2 = 0.0001$
Run 1 uk	21.72	25.46	26.05
Shepp Logan	27.68	28.63	29.70
Generalized Hamming	25.41	23.02	28.66
Hu	34.14	34.70	35.31

Table 6.5 Performance comparison at various noise powers with wavelet pre processing $\rho = 2$

CENTRAL LIBRARY
IIT KANPUR
131212
A

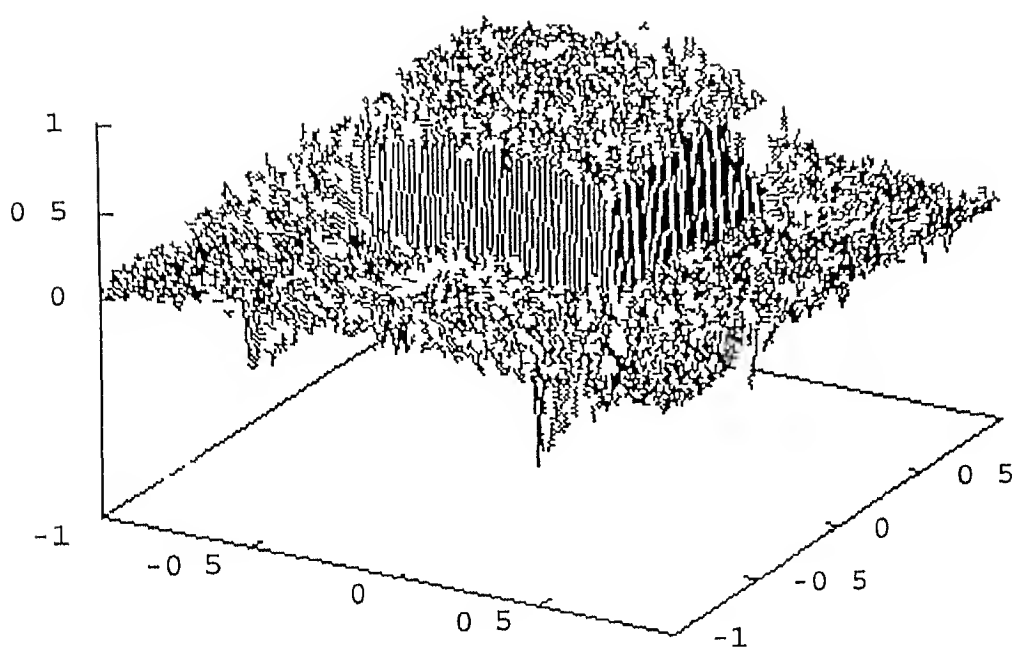


Figure 6.13 Noisy square reconstruction using wavelet pre processing and Ram Lak filter $\rho = 4$

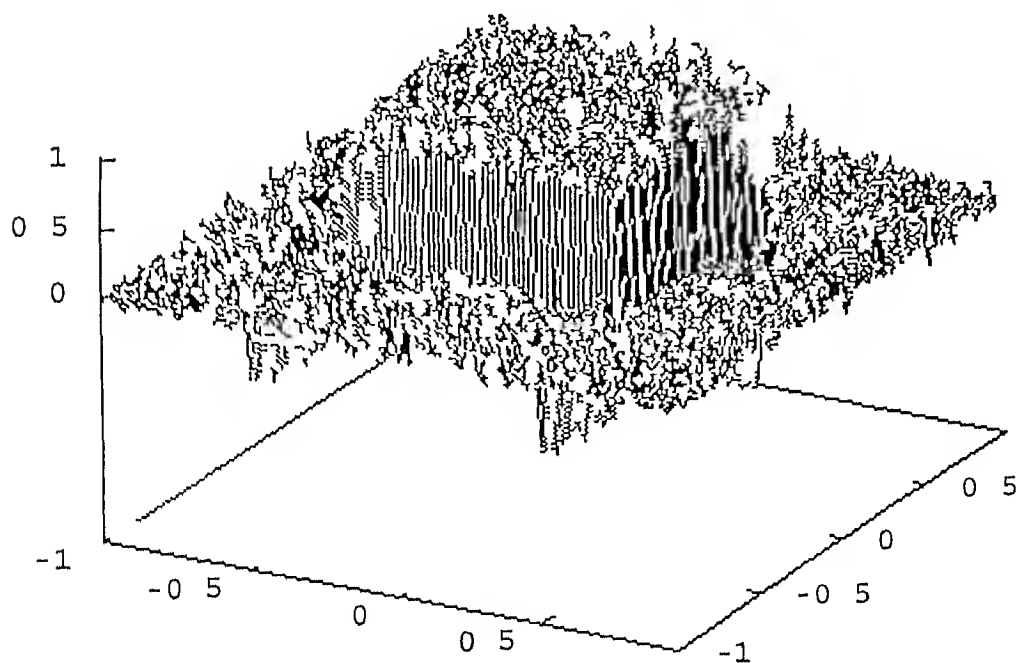


Figure 6.14 Noisy square reconstruction using wavelet pre processing and Shepp Logan filter $\rho = 4$

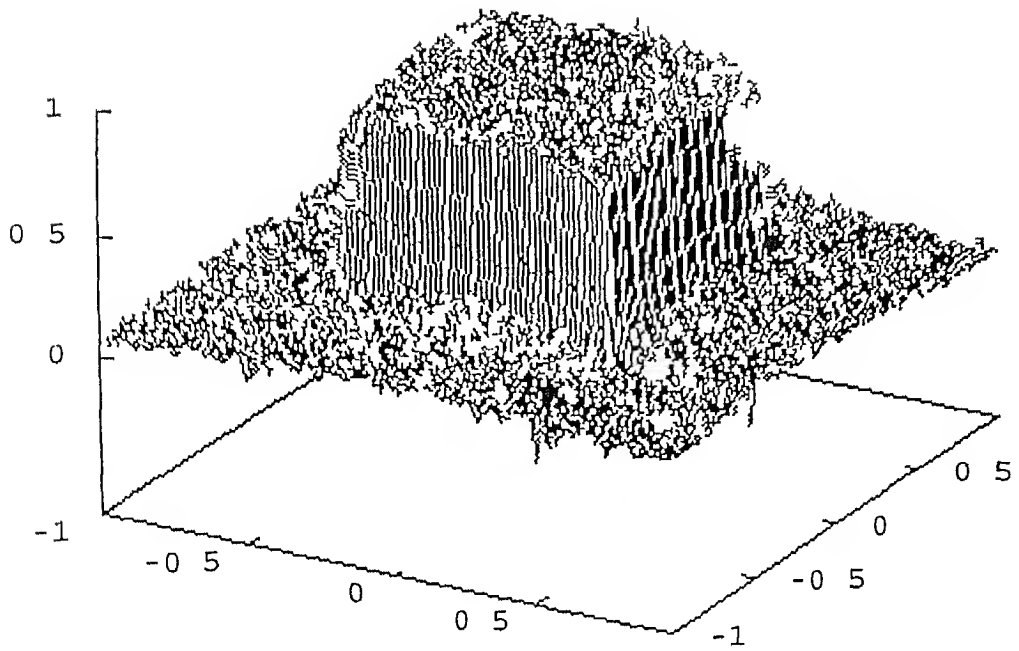


Figure 6.15 Noisy square reconstruction using wavelet pre processing and Generalized Hamming filter $\rho = 4$

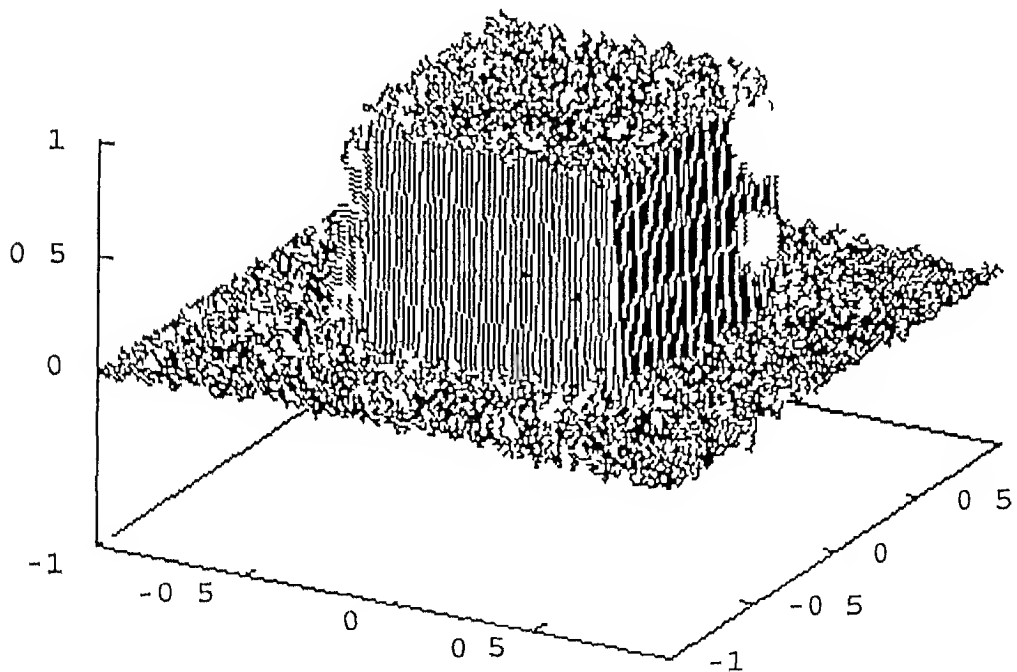


Figure 6.16 Noisy square reconstruction using wavelet pre processing and Haar filter $\rho = 4$

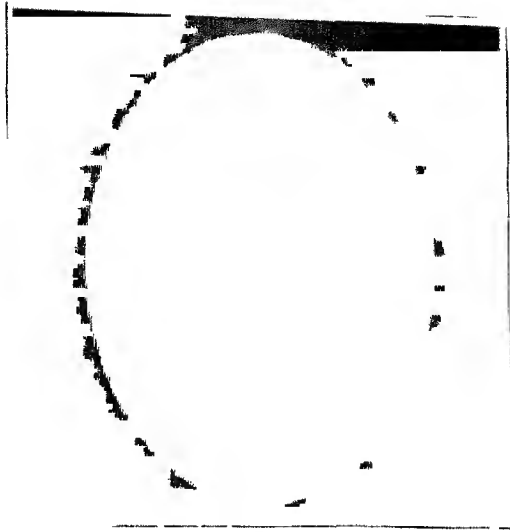


Figure 6 17 Noisy phantom reconstruction using wavelet pre processing and Generalized Hamming filter $\rho = 4$

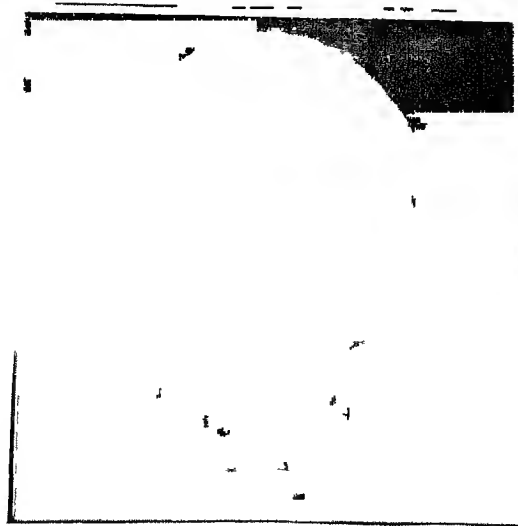


Figure 6 18 Noisy phantom reconstruction using wavelet pre processing and Haar filter $\rho = 4$

Now we consider the performance with constant M/N ratio i.e the no. of projection angles are increased in proportion to the sampling rate in projection domain. The SNR is measured for the square image as well as for the Shepp Logan phantom. For the square image, the Haar filter shows better performance. For Shepp Logan phantom, the Haar filter again gives better results in comparison with the Ram Lak filter. However the performance of Ram Lak improves with increasing N , while Haar filter has shown a small decrease in the SNR value. These results are summarized in table 6.7 & table 6.8

Filter	$\rho = 1, N = 128$	$\rho = 2, N = 256$	$\rho = 4, N = 512$
Ram Lak	30.90	28.34	23.37
Haar		36.87	38.03

Table 6.7 Performance comparison with constant N/M ratio (Using square image)

Filter	$\rho = 1, N = 128$	$\rho = 2, N = 256$	$\rho = 4, N = 512$
Ram Lak	23.26	31.84	46.59
Haar	-	98.71	87.97

Table 6.8 Performance comparison with constant N/M ratio (Using Shepp Logan phantom)

6.3 Conclusion

In this work we have attempted to study the relative performance of different filters used in image reconstruction. The main limitation of Haar filter is that it is not defined for odd values of oversampling ratio. The Haar filter, however, has given improved results for certain class of images such as square images. We feel that for images belonging to a more general class, additional simulation work should be carried out in order to measure the relative performance of Haar filter. Also the Haar filter-wavelet pre processing combination gives better results. These conclusions are based on the results of computer simulations and not based on any kind of analytical treatment.

Appendix A

The $w_{0\Delta}(s, \theta)$, $\theta \in [0, \pi/4]$ has a general trapezoidal shape as shown in fig A 1 where using simple trigonometry we can show that

$$a_\theta = \frac{\Delta}{2}(\cos \theta + \sin \theta) \quad (\text{A } 1)$$

$$b_\theta = \frac{\Delta}{2}(\cos \theta - \sin \theta) \quad (\text{A } 2)$$

$$h_\theta = \frac{\Delta}{\cos \theta} \quad (\text{A } 3)$$

It is shown in [14] that

$$I_{1d}^{-1}(|\xi|) = -\frac{1}{\pi t^2} \quad (\text{A } 4)$$

Hence from eq 3.20 we get

$$k(t, \theta) = -\frac{1}{\pi t^2} * w_{0\Delta}(t, \theta) \quad (\text{A } 5)$$

For the sake of simplicity we will drop the term θ in the discussion to follow and we also assume that $h_\theta = 1$ Hence

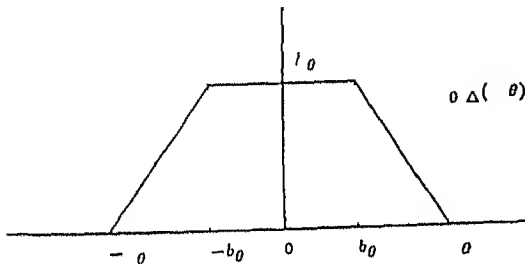


Figure A 1 Geometry of $w_{0\Delta}(s, \theta)$

$$\pi k(t) = - \int_{-\infty}^{\infty} w_{0\Delta}(\tau) \frac{1}{(t-\tau)^2} d\tau \quad (\text{A } 6)$$

Note that $w_{0\Delta}(\tau) = 0$ if $|\tau| > a$ therefore

$$\pi k(t) = - \int_{-b}^{-a} \frac{(\tau + a)}{(a-b)(t-\tau)^2} d\tau - \int_{-b}^b \frac{d\tau}{(t-\tau)^2} - \int_b^a \frac{(a-\tau)}{(a-b)(t-\tau)^2} d\tau \quad (\text{A } 7)$$

$$\begin{aligned} &= \int_{-b}^{-a} \frac{1}{(b-a)} \left[\frac{(t+a)}{(t-\tau)^2} - \frac{1}{(t-\tau)} \right] d\tau - \left[\frac{1}{(t-\tau)} \right]_{-b}^b \\ &\quad + \int_b^a \frac{1}{(b-a)} \left[\frac{(a-t)}{(t-\tau)^2} + \frac{1}{(t-\tau)} \right] d\tau \end{aligned} \quad (\text{A } 8)$$

$$\begin{aligned} &= \frac{(t+a)}{(b-a)} \left[\frac{1}{(t-\tau)} \right]_{-b}^{-a} + \frac{1}{(b-a)} [\ln |t-\tau|]_{-a}^{-b} \\ &\quad - \frac{1}{(t-b)} + \frac{1}{(t+b)} + \frac{(a-t)}{(b-a)} \left[\frac{1}{(t-\tau)} \right]_b^a - \frac{1}{(b-a)} [\ln |t-\tau|]_b^a \end{aligned} \quad (\text{A } 9)$$

$$\begin{aligned} &= -\frac{1}{(t+b)} - \frac{1}{(t-b)} + \frac{1}{(t+b)} + \frac{1}{(t-b)} \\ &\quad + \frac{1}{(b-a)} \left[\ln \frac{|t-b|}{|t-a|} - \ln \frac{|t+a|}{|t+b|} \right] \end{aligned} \quad (\text{A } 10)$$

$$= \frac{1}{(b-a)} \ln \frac{|(t+b)(t-b)|}{|(t+a)(t-a)|} \quad (\text{A } 11)$$

$$= \frac{1}{(a-b)} \ln \frac{|t^2 - a^2|}{|t^2 - b^2|} \quad (\text{A } 12)$$

After substituting the values of a_θ and b_θ as given by eq A 1 , A 2 and multiplying by h_θ we get the final result as

$$k(t, \theta) = \frac{1}{\pi \sin 2\theta} \ln \frac{|t^2 - \frac{\Delta^2}{4}(1 + \sin 2\theta)|}{|t^2 - \frac{\Delta^2}{4}(1 - \sin 2\theta)|} \quad (\text{A } 13)$$

The above discussion is valid for $\theta \neq 0$ The expression for $k(t, 0)$ can be evaluated as a limiting case of the above equation and the result is

$$k(t, 0) = -\frac{\frac{\Delta^2}{2}}{\pi(t^2 - \frac{\Delta^2}{4})} \quad (\text{A } 14)$$

Bibliography

- [1] Deans S R , " The Radon Transform and some of its application", *Wiley Interscience Publication*, 1983
- [2] Herman G T , "Image Reconstruction from projections", *Academic Press*, 1980
- [3] Herman G T , ed , "Image Reconstruction from projections", *Topics in applied physics*, Springer Verlag, 1979
- [4] Jain A K , "Fundamentals of Image Processing", *Prentice Hall International Inc* , 1989
- [5] A H Delaney & Y Bresler "Multiresolution Tomographic Reconstructions using Wavelets " *IEEE Tran on image processing*, Vol 4, No 6, June 1995, pp 799 813
- [6] Y Censor , "Finite Series Expansion Reconstruction Methods " *Proc of IEEE* , Vol 71, No 3, March 1983, pp 409 418
- [7] R M Lewitt , "Reconstruction Algorithms Transform Methods " *Proc of IEEE* , Vol 71, No 3, March 1983, pp 390 408
- [8] Guddon J P and Y Bizais , "Band Limited and Haar Filtered Backprojection Reconstructions " ,*IEEE Trans on medical imaging*, Vol 13, No 3, Sep 1994, pp 430 440
- [9] Sahiner B , Yagle A , "Image Reconstructions from projections under wavelet constraints", *IEEE Trans on Signal Processing*, Vol 41, No 12, December 1993
- [10] Sahiner B , Yagle A , "Reconstruction from projections under Time Frequency constraints", *IEEE Trans on medical imaging*, Vol 14, No 2, June 1995, pp 193 204
- [11] Shepp L A , Logan B T , " The Fourier Reconstruction of a head section", *IEEE Trans on Nuclear Science*, Vol 21, June 1974, pp 21 43

- [12] Mallat S G , "A Theory for Multiresolution Signal Decomposition The Wavelet Representation", *IEEE Trans on Pattern Analysis and Machine Intelligence*, Vol 11, No 7, July 1989
- [13] Mallat S G , "Multifrequency Channel Decomposition of Images and Wavelet Models" *IEEE Trans on ASSP*, Vol 37, No 12, Dec 1989, pp 2091-2110
- [14] B K P Horn , "Density Reconstruction using Arbitrary Ray Sampling Scheme" ,*Proc of IEEE* , Vol 66 No 5 May 1978
- [15] I Daubechies , "The Wavelet Transform, Time Frequency Localization & Signal Analysis " ,*IEEE Trans on Information Theory* ,Vol 36, No 5, Sep 1990, pp 961-1005
- [16] I Daubechies , "Orthogonal Basis of Compactly Supported Wavelets " ,*Comm on Pure and Applied Mathematics* ,Vol 41, No 7, Oct 1988, pp 909-995
- [17] I Daubechies , A Cohen and J C Feauveau , " Biorthogonal Basis of Compactly Supported Wavelets," ,*Comm on Pure and Applied Mathematics* ,Vol 45, No 5, Jun 1992, pp 485-560
- [18] Y I Chian "Wavelet Fundamentals " *Kluwer Academic Press*, 1995
- [19] M Vetterli "A Theory of Multirate Filter Bank", *IEEE Trans on ASSP* , Vol 35, No 3, March 1987, pp 356-372
- [20] Daubechies I , "Ten Lectures on Wavelets", *Society for Industrial and Applied Mathematics*, 1992
- [21] Rioul O, Vetterli M , "Wavelets and Signal Processing", *IEEE Signal Processing Magazine*, Vo 8, No 4, October 1991, pp 14-38
- [22] Papoulis A , "Probability, Random Variables and Stochastic Process", third ed , *Mc Graw Hill Publishers*
- [23] G Vrudhajan , "Image Reconstruction Using Wavelet Transform", *Master's Thesis Dept of EE, IIT Kanpur, Feb 1994*
- [24] Noonan J P , Polchlopek II M , Varteresian M , "A Hypothesis Testing Technique for Wavelet Transform in the presence of Noise", *Digital Signal Processing*, No 3, 1993, pp 89-96

- [25] F. Natterer, "Mathematics of Computerized Tomography", *John Wiley*, 1986

• 121212

121212

Date Slip

This book is to be returned on the
date last stamped

EE-1996-M-705-IMA



A121212